Eur. Phys. J. B (2022)95:38
https://doi.org/10.1140/epjb/s10051-022-00288-y

THE EUROPEAN PHYSICAL JOURNAL B

Regular Article - Solid State and Materials

Structural, elastic, electronic and optical properties of the newly synthesized selenides Tl_2CdXSe_4 (X = Ge, Sn)

S. Karkour[1], A. Bouhemadou[1,a], D. Allali[2], K. Haddadi[3], S. Bin-Omran[4], R. Khenata[5], Y. Al-Douri[6,7], A. Ferhat Hamida[8], A. Hadi[9], and A. F. Abd El-Rehim[10,11]

[1] Laboratory for Developing New Materials and Their Characterizations, Department of Physics, Faculty of Science, University of Ferhat Abbas, Setif 1, 19000 Setif, Algeria
[2] Physics and Chemistry of Materials Lab, Faculty of Science, Department of Physics, University of M'sila, 28000 M'sila, Algeria
[3] Unité de Recherche Matériaux Emergents, University of Ferhat Abbas, Setif 1, 19000 Setif, Algeria
[4] Department of Physics and Astronomy, College of Science, King Saud University, PO Box 2455, Riyadh 11451, Saudi Arabia
[5] Laboratoire de Physique Quantique de la Matière et de Modélisation Mathématique (LPQ3M), Université de Mascara, 29000 Mascara, Algeria
[6] Engineering Department, American University of Iraq-Sulaimani, PO Box 46001, Sulaimani, Kurdistan, Iraq
[7] Department of Mechatronics Engineering, Faculty of Engineering and Natural Sciences, Bahcesehir University, Besiktas, 34349 Istanbul, Turkey
[8] Department of Electronics, University of Ferhat Abbas Setif 1, 19000 Setif, Algeria
[9] Department of Physics, University of Rajshahi, Rajshahi 6205, Bangladesh
[10] Physics Department, Faculty of Science, King Khalid University, PO Box 9004, Abha 61413, Saudi Arabia
[11] Physics Department, Faculty of Education, Ain Shams University, Heliopolis, Roxy, PO Box 5101, Cairo 11771, Egypt

Received 23 October 2021 / Accepted 21 January 2022

Abstract. Motivated by the growing demand for new performant semiconducting materials, we investigated in detail the structural, elastic, electronic and optical properties of two newly synthesized compounds, namely $Tl_2CdGeSe_4$ and $Tl_2CdSnSe_4$, using density functional theory calculations. The calculations were performed relativistically, including the spin–orbit coupling (SOC). The computed equilibrium structural parameters are in excellent agreement with available measurements. Note that the calculations of all the considered properties were performed with the theoretically obtained equilibrium lattice parameters. The predicted monocrystalline and polycrystalline elastic constants reveal that the studied compounds are soft, ductile, mechanically stable and substantially structurally and elastically anisotropic materials. Our calculations using the Tran-Blaha modified Becke-Johnson potential with the inclusion of SOC show that $Tl_2CdGeSe_4$ and $Tl_2CdSnSe_4$ are direct bandgap semiconductors. The inclusion of SOC is found to reduce the fundamental bandgap of $Tl_2CdGeSe_4$ from 1.123 to 0.981 eV and that of $Tl_2CdSnSe_4$ from 1.097 to 0.953 eV. The *l*-decomposed atom-projected densities of states were calculated to identify the contribution of each constituent atom to the electronic states in the energy bands. The upper valence subband predominantly comes from the Se-4*p* states, while the bottom of the conduction band mainly originates from the Se-4*p* and Ge-4*p*/Sn-5*p* states. The frequency-dependent linear optical parameters, viz., the complex dielectric function, absorption coefficient, refractive index, reflectivity and energy-loss function, were calculated for electromagnetic waves polarized parallel and perpendicular to the *c*-axis in a wide energy window. An attempt was made to identify the microscopic origin of the peaks and structures observed in the calculated optical spectra.

1 Introduction

One current challenge in research is to identify new semiconductors with valuable properties that can meet the requirements of the rising demand for efficient optoelectronic devices. For this purpose, chalcogenide

[a] e-mails:a_bouhemadou@yahoo.fr; abdelmadjid_bouhemadou@univ-setif.dz(corresponding author)

Published online: 01 March 2022

semiconductors involving copper/silver and alkali metals (AM) have attracted significant research interest stimulated by the fact that their properties, such as diverse stable crystal structures, compositional flexibility, high thermal stability, semiconductivity, photovoltaic effects, highly efficient nonlinear optics and favorable thermoelectricity, are appropriate for efficient applications in photovoltaic cells, optoelectronics and nonlinear optical devices [1–14]. Therefore, the synthesis and characterization (experimentally and theoretically) of new alkali metal-based chalcogenides has become a very active research area. Many synthesized AM-based chalcogenides possess interesting properties that make them potential candidates for useful applications [7]. Unfortunately, in addition to their interesting useful properties, there are concerns about AM-based chalcogenides. For instance, their low electronegativity and reactivity may hinder their technological applications. The first drawback, namely, their low electronegativity, may lead to large bandgaps and greater diffusion of charge carriers. The second disadvantage, namely, reactivity, can lead to instability under exposure to air or humidity. It is believed that replacing the AM atom with an atom of another element of similar chemistry could retain the advantageous properties of AM-based chalcogenides while overcoming their disadvantages [15]. One interesting candidate for this purpose is thallium (Tl) because the chemistry of the Tl^{1+} cation is similar to that of alkali metals; Tl can behave as a pseudo-AM [16, 17]. Furthermore, Tl has some properties that may lead Tl-containing systems to avoid the disadvantages of alkali metal-based compounds. First, Tl is much less electropositive than alkali metals; the electronegativity of Tl (2.04) is much higher than that of any alkali metal element. This leads to a less ionic character in Tl-based compounds, which may lead to smaller bandgaps and consequently to low electrical resistivities and, therefore, to higher carrier mobilities. Second, Tl is heavier than any stable alkali metal, which results in low lattice thermal conductivity and thus improves physical properties requiring low lattice thermal conductivity such as thermoelectric efficiency. Third, T^{l+} has a lone pair of electrons that can be stereoactive; therefore, Tl-containing materials tend to be less sensitive to air and moisture than AM-based compounds [17]. Fourth, the substitution of an alkali metal atom for a T1 atom in a material can result in an isostructural compound. Due to the advantages mentioned above, significant research has been devoted to the exploration of Tl-based chalcogenides which may be alternatives to chalcogenides containing alkali metals. Despite numerous reports on the synthesis and crystal structure characterizations of a series of Tl-based quaternary chalcogenides, such as $Tl_2B^{II}C^{IV}X_4$ (B^{II} = Mn, Cd, Hg, Pb; D^{IV} = Si, Ge, Sn; X = S, Se, Te) systems [16–27], the research on these materials is still insufficient. Hence, they are of current interest.

Recently, data on the crystal structure, formation conditions and measured absorption coefficient spectrum of dithallium cadmium germanium selenide $Tl_2CdGeSe_4$ [24, 27] and dithallium cadmium tin selenide $Tl_2CdSnSe_4$ [19, 24, 25] have been reported. In addition, the results of ab initio calculations of the band structure and optical coefficients have been reported for $Tl_2CdSnSe_4$ and $Tl_2CdGeSe_4$ crystals [25, 27]. Previous studies [25, 27] coupling experimental and theoretical approaches to explore synthesis, electronic structure and optical constants have led to the conclusion that the quaternary selenides $Tl_2CdSnSe_4$ and $Tl_2CdGeSe_4$ could be very promising compounds for solar cell applications in thin films and optoelectronics [25]. It is well known that thorough knowledge and understanding of the fundamental properties of a material, such as the structural, elastic, electronic and optical properties, are the key to predicting the possible uses of that material for particular technological applications [28]. To the best of our knowledge, the elastic properties of $Tl_2CdGeSe_4$ and $Tl_2CdSnSe_4$ have not yet been explored, experimentally or theoretically. In addition, in-depth theoretical exploration of the electronic and optical properties of $Tl_2CdSnSe_4$ and $Tl_2CdSnSe_4$ is still far from complete. To fill this gap, we explored in detail the structural, elastic, electronic and optical properties of the newly synthetized materials $Tl_2CdGeSe_4$ and $Tl_2CdSnSe_4$ using two complementary density functional theory (DFT) methods, namely, the pseudopotential plane wave (PP-PW) and full-potential (linearized) augmented plane wave plus local orbitals (FP-(L)APW + lo) methods. Note that calculations based on DFT are becoming a powerful tool for predicting the fundamental properties of materials and their implications in applications. DFT is not only useful for theoretical studies but also is well integrated for applied studies [29–31].

The outline of the paper is as follows: The computational settings used are presented in the following section. The presentation and discussion of the obtained results including the crystal structure, elastic moduli, electronic structure and optical coefficients and functions are the subjects of Sects. 3.1, 3.2, 3.3 and 3.4, respectively. The last section; Sect. 4, summarizes our findings.

2 Calculation methods and settings

Quantum–mechanical calculations of the optimized structural parameters and monocrystalline elastic constants, C_{ij}, were performed using an efficient method to relax the crystal structure, namely the pseudopotential plane wave (PP-PW) approach based on density functional theory (DFT) as incorporated in the Cambridge Sequential Total Energy Package (CASTEP) [32]. The exchange–correlation interactions were modeled using the PBEsol form of the general gradient approximation (labeled GGA-PBEsol or GGA-08) [33], which was specially developed to better predict the optimized crystal structures of solids. Norm-conserving pseudopotentials [34, 35] were used to describe the Coulombic interactions between the valence electrons and ion cores. The electron states Tl: $5d^{10}6s^26p^1$, Cd: $4s^24p^64d^{10}5s^2$, Sn:

$4d^{10}5s^25p^2$, Ge: $3d^{10}4s2\ 4p^2$ and Se: $3d^{10}4s^24p^4$ were treated as the valence states. The Kohn–Sham electronic wave functions were developed on a plane wave basis set truncated at an energy cutoff of 1350 eV. Integrations over the Brillouin zone (BZ) were performed over a 7 × 7 × 6 special Monkhorst–Pack k-mesh [36]. The Broyden–Fletcher–Goldfarb–Shanno (BFGS) technique [37] was employed to relax the free structural parameters, viz., the Se internal coordinates, x_{Se}, y_{Se}, z_{Se}, and the lattice parameters, a and c, with convergence cutoffs of 5.0×10^{-6} eV/atom, 0.01 eV/Å, 0.02 GPa and 5.0×10^{-4} Å for the total energy, maximum ionic Hellmann–Feynman force, maximum ionic displacement and maximum stress, respectively. The well-known stress–strain technique [32] was used to calculate the monocrystalline elastic constants C_{ij}. In this approach, C_{ij} is estimated by computing the stress tensors $\overleftrightarrow{\sigma}$ generated by applying different small deformation tensors $\overleftrightarrow{\delta}$ to the equilibrium lattice, and then C_{ij} is determined by a linear fit of the computed stress–strain curves. Two deformations, where the first is defined by a strain tensor $\overleftrightarrow{\delta}$ with only two nonzero components, viz., δ_{xx} and δ_{yz}, and the second with also only two non-zero components, viz.,δ_{zz} and δ_{xy}, are sufficient to determine the six independent elastic constants, namely, C_{11}, C_{33}, C_{44}, C_{66}, C_{12} and C_{13}, of a tetragonal system. The phonon-dispersion curves were calculated through a linear-response method based on density functional perturbation theory [37].

Calculations of the electronic and optical properties were carried out through the full-potential (linearized) augmented plane wave plus local orbitals (FP-L/APW + lo) as implemented in the WIEN2k code [38]. The FP-(L)APW + lo method is one of the most accurate approaches for calculating electronic structure and the associated properties. It is well established that the energy bandgap calculated through common exchange–correlation (XC) functionals, namely the local density approximation (LDA) and the generalized gradient approximation (GGA), are generally significantly smaller than that from experimental data. Thus, some XC functionals beyond the standard LDA and GGA, such as hybrid functionals, the GW method and the Tran-Blaha-modified Becke-Johnson (TB-mBJ) potential, have been developed to overcome this deficiency. To remedy the systematic underestimation of the bandgap by the GGA, we used the TB-mBJ potential [39, 40], which has been shown to predict bandgaps that are in good agreement with experimental counterparts and with theoretical results obtained using more advanced calculations, such as those based on Green's function (GW) and hybrid functionals, for a wide variety of semiconductors and insulation [41–44]. Note that the computation cost when using the TB-mBJ potential is significantly lower than that when using the hybrid functionals and GW approximation [45]; the computation time using the TB-mBJ potential is comparable to that using the standard LDA and GGA. Therefore, TB-mBJ was chosen to correct the bandgaps of the studied Tl-based selenides. The valence wave functions inside the interstitial region were developed on a plane wave basis set, with the largest k vector ($K_{\max}$) equal to $9/R_{MT}^{\min}$, where $R_{MT}^{\min}$ is the smallest muffin-tin radius in the Bohr unit. The valence wave functions inside the muffin-tin spheres were developed on spherical harmonics up to $l_{\max} = 10$. The muffin-tin sphere radius was chosen to equal 2.5 Bohr for Tl, 2.46 Bohr for Cd, 2.14 Bohr for Ge, 2.35 Bohr for Sn and 2.14 Bohr for Se. The total energy convergence was set to 10^{-5} Ry, and the atom relaxation was determined with a force on each atom less than 0.1 eV/Å.

The optical properties of a material affect the characteristics of electromagnetic waves passing through it by modulating their propagation vector (dispersion) or intensity (absorption). The linear macroscopic response of a solid medium to incident electromagnetic waves is modeled by the optical complex dielectric function $\varepsilon(\omega) = \varepsilon_1(\omega) + \varepsilon_2(\omega)$, where $\varepsilon_1(\omega)$ (the real part) models the dispersion of electromagnetic radiation and $\varepsilon_2(\omega)$ (the imaginary part) models the dissipation of the energy of electromagnetic radiation inside the crossed medium. Theoretically, the $\varepsilon_2(\omega)$ spectrum is calculated by summing all the individual contributions of the allowed direct electronic transitions between the pairs of electronic states (V_n, k) and ($C_{n'}$, k), where (V_n, k) is an occupied electronic state in a valence band of index n and ($C_{n'}$, k) is an unoccupied electronic state in a conduction band of index n'. The spectrum of the dispersive part of the dielectric function, $\varepsilon_1(\omega)$, is then computed from the $\varepsilon_2(\omega)$ spectrum through the Kramers–Kronig transformation. The spectra of the other macroscopic linear optical functions, namely, the refractive index $n(\omega)$, extinction coefficient $k(\omega)$, optical reflectivity $R(\omega)$, absorption coefficient $\alpha(\omega)$ and energy-loss function $L(\omega)$, can be computed from the $\varepsilon_1(\omega)$ and $\varepsilon_2(\omega)$ spectra. All the reported spectra of macroscopic linear optical functions in this work were calculated using the random phase approximation formulation developed by Ambrosch–Draxl and Sofo [46] and implemented in the WIEN2k code. A large grid of $40\times40\times40$ k-points was used to calculate the electronic properties and optical spectra, as they are very sensitive to the k-mesh. Due to the presence of heavy atoms in the studied compounds, all the performed calculations were carried out both with and without spin–orbit coupling, which we refer to hereafter as + SOC and NSOC, respectively.

3 Results and discussion

This section is devoted to the presentation and discussion of the obtained results concerning the structural, elastic, electronic and optical properties of the Tl-containing selenides: $Tl_2CdGeSe_4$ and $Tl_2CdSnSe_4$.

3.1 Equilibrium structural parameters

The investigated isostructural compounds, $Tl_2CdGeSe_4$ and $Tl_2CdSnSe_4$, crystallize in the tetragonal system

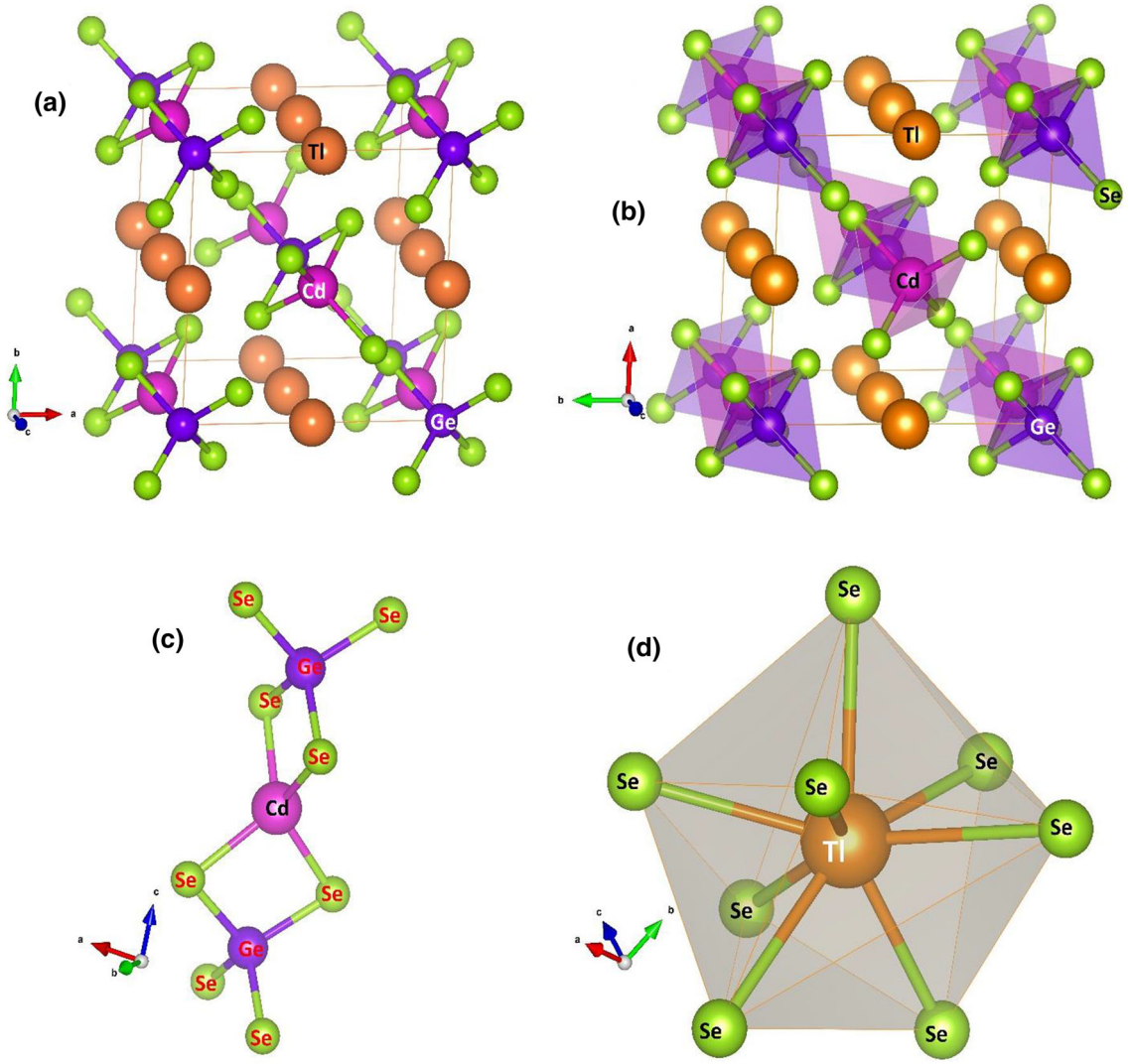

Fig. 1 **a** A view of the $Tl_2CdGeSe_4$ unit cell structure, **b** Cd- and Ge-centered polyhedral representation in a unit cell, **c** the nearest surrounding of Cd and Ge atoms by Se atoms ($CdSe_4$ and $GeSe_4$ tetrahedra), **d** the nearest surrounding of Tl atoms by Se atoms

with the noncentrosymmetric space group I-42 m (No. 121), as determined through X-ray diffraction analysis [19, 24, 25]. The location and coordination of the surrounding atoms constituting the unit cell structure of $Tl_2CdGeSe_4$, as a representative, are depicted in Fig. 1. The Cd and Ge atoms, which are bonded to four Se atoms forming slightly distorted tetrahedra (see the polyhedral diagrams in Fig. 1b, c), occupy Wyckoff sites 2b (0, 0, 0.5) and 2a (0, 0, 0), respectively. The Tl atom, which is coordinated by eight Se atoms forming a distorted tetragonal antiprism (Fig. 1d), is locates at Wyckoff site 4c (0, 0.5, 0). The Se atom, which is surrounded by 1Cd, 1Sn and 4Tl cations forming a trigonal prism, occupies Wyckoff site 8i (x_{Se}, x_{Se}, z_{Se}), where x_{Se}, x_{Se} and z_{Se} are the internal coordinates of the Se atom. Thus, the crystal structure of the studied compounds has four free structural parameters not fixed by the space group, namely the following: the cell parameters, a and c, and the internal coordinate, x_{Se} and z_{Se}, which have to be relaxed to reach the equilibrium crystal structure. The equilibrium structural parameters of the studied compounds, viz., the lattice parameters, a and c, the internal coordinates of the Se atom and the distances between the nearest neighbors, computed both with and without spin–orbit coupling (labeled + SOC and NSOC, respectively), are presented in Tables 1 and 2 along with the available corresponding measured values [19, 24, 25]. Our calculated values for the lattice parameters and the corresponding experimental data [1, 24, 25] demonstrate excellent agreement; the maximum relative discrepancy does not exceed − 0.8% when spin–orbit coupling is included. The calculated relaxed fractional internal coordinates of the Se atom and bond lengths are also consistent with the available corresponding experimental data.

Table 1 Calculated equilibrium lattice parameters (a and c, in Å), unit cell volume (V, in Å^3), relative deviation of the computed values from the corresponding experimental data (d%) and relaxed fractional internal coordinates of the Se atom (x/a, y/b z/c) for the $Tl_2CdGeSe_4$ and $Tl_2CdSnSe_4$ compounds. Available results in the literature for the investigated compounds are tabulated for the sake of comparison. + SOC (NSOC) refers to calculations performed with (without) including spin–orbit coupling (SOC)

System	a	d (%)	c	d (%)	V	d (%)	$Se_{x/a}$	$Se_{y/b}$	$Se_{z/c}$
$Tl_2CdGeSe_4$									
Present									
NSOC	7.8739	− 1.7	6.7256	0.03	416.976	− 3.5	0.1713	0.1713	0.2166
+ SOC	7.9453	− 0.8	6.7107	− 0.2	423.632	− 1.9	0.1689	0.1689	0.2185
Expt. [24]	8.0145		6.7234		431.859		0.1641	0.16410	0.2819
Other [27]	8.4502	5.4	6.7740	0.4	483.703	12.2	0.16044	0.16044	0.28758
$Tl_2CdSnSe_4$									
Present									
NSOC	7.9125	− 1.6	6.8216	− 0.5	427.084	− 3.8	0.1759	0.1759	0.2275
+ SOC	7.9888	− 0.7	6.8651	0.1	438.137	− 1.3	0.1762	0.1762	0.2352
Expt. [24]	8.0480[2]		6.8569		444.123		0.1742	0.1742	0.240
[19]	8.0490[1]		6.8573		444.260		0.1713	0.1713	0.2520
Theor. [25]	8.1673	1.5	6.9405	1.2	462.964	4.2	0.1761	0.1761	0.2366

Table 2 Calculated equilibrium interatomic distances (d, in Å), number of identical bonds (N.B.) and coordination numbers (C.N.) of atoms in the $Tl_2CdGeSe_4$ and $Tl_2CdSnSe_4$ with including spin–orbit coupling, compared to available data in literature

$Tl_2CdGeSe_4$				$Tl_2CdSnSe_4$			
Atom	Bond (N.B.)	d (Å)	C.N.	Atom	Bond (N.B.)	d (Å)	
Tl	Tl–Se (4)	3.2972[1]3.336[2]	8	Tl	Tl–Se (4)	3.3572[1]3.42[2]; 3.433[3]	8
	Tl–Se (4)	3.5055[1]3.545[2]			Tl–Se (4)	3.45453.453[2]; 3.447[3]	
Cd	Cd–Se (4)	2.6777[1]2.65[2]	4	Cd	Cd–Se (4)	2.6933[1]2.58[2]; 2.587[3]	4
Ge	Ge–Se (4)	2.3986[1]2.368[2]	4	Sn	Sn–Se (4)	2.5673[1]2.63[2]; 2.605[3]	4
Se	Se–Ge (1)	2.3986[1]0.2368[2]	6	Se	Se–Sn (1)	2.5673[1]2.63[2]; 2.605[3]	6
	Se–Cd (1)	2.6777[1]2.65[2]			Se–Cd (1)	2.6933[1]2.58[2]; 2.587[3]	
	Se–Tl (2)	3.2972[1]0.3336[2]			Se–Tl (2)	3.3572[1]3.42[2]; 3.433[3]	
	Se–Tl (2)	0.3505[1]0.3545[2]			Se–Tl (2)	3.4545[1]3.453[2]; 3.447[3]	

[1]Present
[2]Expt. [24]
[3]Expt. [19]

This excellent consistency between the calculated values and the experimental counterparts confirms the reliability of the PP-PW method to predict the optimized structural geometry. Note that the unit cell parameters of $Tl_2CdSnSe_4$ are somewhat larger than those of $Tl_2CdGeSe_4$. Since all constituent atoms except D^{IV} (D^{IV} = Ge, Sn) are the same, the increase in unit cell volume when Sn substitutes for Ge is attributed to the fact that the atomic radius of the Sn atom ($R = 2.81$ Å) is somewhat larger than that of the Ge atom ($R = 2.45$ Å).

To check the dynamic stability of the title compounds, the phonon-dispersion curves along the high symmetry lines in the Brillouin zone were calculated for both compounds. As seen from the phonon-dispersion curve of $Tl_2CdGeSe_4$ represented in Fig. 2, the dispersion branches have positive frequencies at any vector, suggesting that the compounds of interest are dynamically stable.

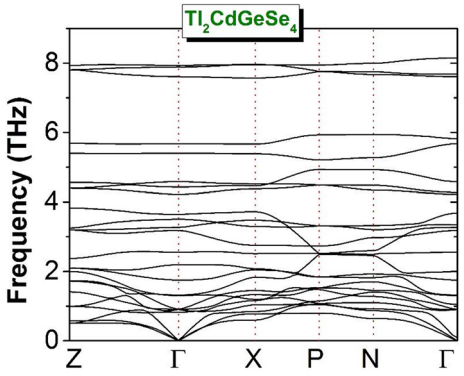

Fig. 2 Calculated phonon dispersion along the high-symmetry lines in the Brillouin zone for $Tl_2CdGeSe_4$

Table 3 Calculated monocrystalline elastic constants (C_{ij}, in GPa) for the $Tl_2CdGeSe_4$ and $Tl_2CdSnSe_4$ compounds with (+ SOC) and without (NSOC) including spin–orbit coupling

System	C_{11}	C_{33}	C_{44}	C_{66}	C_{12}	C_{13}
$Tl_2CdGeSe_4$						
NSOC	46.1	75.0	16.3	13.6	19.2	19.1
+SOC	35.8	67.3	9.8	9.6	12.8	13.9
$Tl_2CdSnSe_4$						
NSOC	46.4	74.8	11.0	11.8	17.8	17.8
+ SOC	40.3	67.4	13.2	14.4	15.2	14.4

3.2 Elastic parameters

3.2.1 Monocrystalline elastic constants

The monocrystalline elastic constants C_{ij} mirror the extent of the crystals' ability to recover their original shape after the stress is removed within the elastic limit, so they are key mechanical parameters of crystals. The C_{ij} values are closely related to a wide range of fundamental solid-state properties, such as mechanical stability, phonon dispersion, heat capacity, Debye temperature, Grüneisen parameter, thermal expansion, the character and strength of the interatomic bonds, elastic wave velocities and melting point. Thus, it is of fundamental and practical interest to evaluate the C_{ij} values of a crystal using reliable theoretical approaches and precise experimental techniques. We are not aware of any experimental or theoretical determination of the C_{ij} values for the compounds of interest; hence, our results, listed in Table 3, are the first numerical assessment. From the predicted C_{ij} values, information on the elastic and mechanical properties can be extracted.

(i) The computed C_{ij} values fulfill all the necessary conditions for the mechanical stability of a tetragonal crystal [47]: $C_{11} > |C_{12}|$; $2C_{13}^2 < C_{33}(C_{11} + C_{12})$; $C_{44} > 0$; $C_{66} > 0$. Thus, $Tl_2CdGeSe_4$ and $Tl_2CdSnSe_4$ are mechanically stable.

(ii) The C_{11} value, which reflects the resistance to linear compression or elongation of the crystal along the a-axis, is noticeably smaller than the C_{33} value, which mirrors the resistance to linear compression or elongation along the c-axis, indicating that the studied compounds show higher stiffness against strains along the c-axis than against strains along the a-axis. This suggests that under the same perpendicular uniaxial stress, the crystal is more compressible along the a-axis than along the c-axis; thus, the linear compressibility is dependent on the crystal direction. This result indicates that the interatomic bonds along the a-axis are weaker than those along the c-axis.

(iii) The C_{11} and C_{33} values are noticeably larger than those of C_{12}, C_{13}, C_{44} and C_{66}, which characterize the resistance to shear deformations, indicating that the studied compounds are more resistant to compression than to shear.

(iv) He velocities of sound waves propagating along the main crystal directions can be deduced from the monocrystalline elastic constants. The formulas used and the obtained results for the velocities of sound waves propagating along the [100]/[010], [110] and [001] crystallographic directions are listed in Table 4. Table 4 shows that the sound wave velocities depend considerably on their own polarizations and on the crystal directions. The noticeable differences between the velocities of the sound waves propagating in the considered principal directions constitute proof of the considerable elastic anisotropy of the compounds of interest. The longitudinally polarized sound wave propagating along the [001] crystallographic direction is the fastest. The sound wave velocity is closely linked to the lattice thermal conductivity; the lower the sound velocity is, the lower the lattice thermal conductivity. The relatively low values of the anisotropic sound wave velocities suggest that the lattice thermal conductivities of both considered compounds are lower.

3.2.2 Polycrystalline elastic moduli

Generally, the synthetized samples are polycrystalline aggregates of single-phase monocrystals with random orientation; therefore, it is not possible to measure the C_{ij} values in this case, but instead, we can measure the isotropic bulk modulus B (which reflects the resistance to volume change under the hydrostatic pressure effect) and the shear modulus G (which characterizes the resistance to shape change under the influence of shear force). Theoretically, it is possible to calculate the isotropic elastic moduli B and G of a material from

Table 4 Computed velocities (in ms^{-1}) of the anisotropic sound waves propagating in the [100], [110] and [001] crystallographic directions in the monocrystals $Tl_2CdGeSe_4$ and $Tl_2CdGeSe_4$, isotropic longitudinal, transversal and average sound velocities (V_l, V_t and V_m, in ms^{-1}), and Debye temperature (T_D, in K) for the polycrystalline aggregates $Tl_2CdGeSe_4$ and $Tl_2CdSnSe_4$. The mass density ρ is equal to 7.1307 g/cm^3 for $Tl_2CdGeSe_4$ and 7.2670 g/cm^3 for $Tl_2CdSnSe_4$. L and T refer to longitudinal and transversal polarizations of the sound wave, respectively. Calculations were performed with including spin–orbit coupling

Direction	Polarisation	Formula	$Tl_2CdGeSe_4$	$Tl_2CdSnSe_4$
[100]	[100] (L)	$\sqrt{C_{11}/\rho}$	2241	2355
	[010] (T1)	$\sqrt{C_{66}/\rho}$	1160	1408
	[001] (T2)	$\sqrt{C_{44}/\rho}$	1172	1348
[110]	[110] (L)	$\sqrt{(C_{11}+C_{12}+2C_{66})/2\rho}$	2180	2928
	[1$\bar{1}$0](T1)	$\sqrt{(C_{11}-C_{12})/2\rho}$	1613	1727
	[001] (T2)	$\sqrt{C_{44}/\rho}$	1172	1348
[001]	[001] (L)	$\sqrt{C_{33}/\rho}$	3084	3045
	(001) plane (T)	$\sqrt{C_{44}/\rho}$	1172	1348
V_l			1286	1422
V_t			2346	2494
V_m			1504	1573
T_D			150	155

Table 5 Predicted Reuss, Voigt and Hill bulk (B_R, B_V and B_H, in GPa) and shear (G_R, G_V and G_H, in GPa) moduli, Hill Young's modulus (E_H, in GPa) and Hill Poisson's ratio (σ_H, dimensionless) for the polycrystalline aggregates $Tl_2CdGeSe_4$ and $Tl_2CdSnSe_4$. + SOC (NSOC) refers to calculations performed with (without) including spin–orbit coupling (SOC)

System	B_V	B_R	B_H	G_V	G_R	G_H	E_j			E_H	σ_H
							E_x	E_y	E_z		
$Tl_2CdGeSe_4$											
NSOC	31.3	30.0	30.6	16.6	15.8	16.2	36.2	36.2	63.9	16.2	0.275
+ SOC	24.5	22.6	23.5	12.4	11.3	11.8	30.0	30.0	56.4	30.4	0.285
$Tl_2CdSnSe_4$											
NSOC	30.5	29.3	29.9	14.4	13.1	13.9	37.74	37.74	64.87	35.8	0.300
+ SOC	26.2	25.0	25.6	15.1	14.4	14.7	33.32	33.32	59.39	37.1	0.259

its elastic constants (C_{ij} values) and compliance constants (S_{ij} values) via Voigt–Reuss–Hill (VRH) approximations [48]. With the Voigt approximation, in which a uniform strain is assumed throughout the polycrystal, the upper limits of B and G, viz., B_V and G_V, can be evaluated, while through the Reuss approximation, which is based on an assumption of uniform stress, we can estimate the lower limits of B and G, viz., B_R and G_R. Hill's approximation [48] assumes that the arithmetic mean of the Voigt and Reuss limits constitutes the best theoretical value for the polycrystalline modulus of elasticity. B_V, G_V, B_R, G_R, B_H and G_H, where the subscripts V, R and H denote the Voigt, Reuss and Hill approximations, respectively, are given by the following relationships [49, 50]:

$$B_V = (1/9)[C_{11}+C_{22}+C_{33}+2(C_{12}+C_{13}+C_{23})],$$

$$G_V = (1/5)[C_{11}+C_{22}+C_{33}+3(C_{44}+C_{55}+C_{66})-(C_{12}+C_{13}+C_{23})],$$

$$1/B_R = (S_{11}+S_{22}+S_{33})+2(S_{12}+S_{23}+S_{13}),$$

$$1/G_R = (4/15)[(S_{11}+S_{22}+S_{33}) -(4/15)(S_{12}+S_{13}+S_{23}) +(1/5)(S_{44}+S_{55}+S_{66})],$$

$$B_H = \frac{B_V+B_R}{2}; G_H = \frac{G_V+G_R}{2}.$$

In addition, Young's modulus E, which reflects the resistance of a material to uniaxial stresses; defined as the ratio of the vertically applied linear stress and the linear strain, and Poisson's ratio σ, which mirrors the tendency of a material to expand or contract in a direction perpendicular to a loading direction, given by the

negative value of the ratio of the transverse strain (vertical to the applied stress) to the longitudinal strain (in the direction of the applied stress), can be numerically estimated through the following relationships:

$$E = \frac{9BG}{3B+G}; \sigma = \frac{3B-2G}{2(3B+G)}.$$

The values of the isotropic elastic moduli B, G, E and σ deduced from the predicted C_{ij} values are gathered in Table 5. From the obtained results, we can obtain the following information:

(i) The isotropic elastic moduli B, G and E have relatively small values, reflecting the low hardness and stiffness of the considered materials. Hardness is an important mechanical property that is defined as the resistance of a material to localized deformation [32, 51]. The calculated Vickers hardness ($\simeq$ 3.30 GPa for $Tl_2CdGeSe_4$ and $\simeq$ 2.42 GPa for $Tl_2CdSnSe_4$) confirms the low hardness of these materials.

(ii) The B value is practically double that of G, suggesting that shear deformation can occur more easily than volume change and that G is the decisive elastic modulus affecting the mechanical stability of the title compound [52].

(iii) Poisson's ratio (σ) is often used as a useful indicator of plasticity in materials. Indeed, from the σ value, we can predict whether a material is ductile or brittle. When the σ value is greater than 0.26, the material is predicted to be ductile, and when it is lower than this 0.26, the material is brittle [53]. According to this indicator, $Tl_2CdGeSe_4$ is rather ductile, while $Tl_2CdSnSe_4$ is on the border between ductile and brittle. Based on the fact that the shear modulus G mirrors the resistance to plastic deformation and the bulk modulus B mirrors the resistance to fracture, another empirical indicator claims that the quotient of B and G (B/G) of the polycrystalline phase can provide information about plasticity in materials [54]. According to this indicator, a compound is ductile in nature if the B/G ratio is greater than 1.75; otherwise, it is brittle in nature. Our predicted B/G ratio values, B/G $\simeq$ 2.08 for $Tl_2CdGeSe_4$ and B/G $\simeq$ 1.74 for $Tl_2CdSnSe_4$, confirm the results already obtained through Poisson's ratio, i.e., that $Tl_2CdSnSe_4$ is ductile and $Tl_2CdSnSe_4$ is on the border between ductility and brittleness. A ductile material is easily machinable and resistant to thermal shock.

(iv) The typical value of Poisson's ratio for a covalent material is $\simeq$ 0.2, while it is in the range of 0.3–0.4 for an ionic material and equal to 0.5 for the pure-ionic limit [55]. Based on these criteria, $Tl_2CdGeSe_4$, with $\sigma \simeq 0.285$, and $Tl_2CdGeSe_4$, with $\sigma \simeq 0.259$, exhibit a mixture of covalent and ionic interatomic bonds, but the ionic character is dominant.

(v) The Debye temperature T_D, which is closely related to the thermal parameters of solids, can be predicted from the average velocity of the elastic wave (V_m), which can be numerically estimated from the B and G values [55, 56]. The predicted V_m and T_D values are presented in Table 4. A high Debye temperature mirrors a high associated thermal conductivity [57]. These low values of V_m and T_D denote a low thermal conductivity for the studied compounds.

3.2.3 Elastic anisotropy

Microcracks and mechanical failures can occur in crystals with notable elastic anisotropy [58]. Thus, it is essential to analyze the extent of elastic anisotropy to understand its mechanism and possibly find a procedure to improve the mechanical properties of crystals to avoid the drawbacks of elastic anisotropy. A variety of experimental and theoretical metrics have been established to quantify the extent of elastic anisotropy in materials [59]. Here, we used five different ways to probe the degree of elastic anisotropy in the studied materials.

i. Since the shear modulus G is a key elastic parameter for the mechanical stability of materials, we start by evaluating the extent of the shear anisotropy through the calculation of the shear anisotropic factors A_1, A_2 and A_3. For a tetragonal system, $A_1 = A_2$. The shear anisotropic factor $A_1 = A_2$, which characterizes the anisotropy of shear caused by the application of a stress on the crystallographic planes {001} along the crystallographic directions $< 011 >$ (symbolized by $< 011 > \{100\}$) and along the directions $< 010 >$ (symbolized by $(< 010 > \{100\})$, is defined as: $A_1 = A_2 = 4C_{44}/(C_{11}+C_{33}-2C_{13})$. The shear anisotropic factor A_3, which characterizes the anisotropy of the $< 110 > \{001\}$ and $< 010 > \{001\}$ shear, is given by $A_3 = 2C_{66}/(C_{11} - C_{12})$ [58, 60]. For isotropic shear, the corresponding anisotropic factor is equal to unity. Thus, the degree of deviation of the anisotropy factors from unity reflects the elastic anisotropy degree of the crystal. The calculated values for A_1/A_2 and A_3 are equal to 0.52 and 0.84 (0.67 and 1.15), respectively, for $Tl_2CdGeSe_4$ ($Tl_2CdSnSe_4$), suggesting that these compounds are characterized by a large shear anisotropy.

ii. The ratio of the linear compressibility along the c-axis (β_c) to the linear compressibility along the a-axis (β_a), defined as [60] $\beta_c/\beta_a = ((C_{11} - C_{13}) + (C_{12} - C_{13}))/(C_{33} - C_{13})$, is usually used to assess the degree of elastic anisotropy in crystals. The calculated β_c/β_a ratios are equal to 0.39 for $Tl_2CdGeSe_4$ and 0.52 for $Tl_2CdSnSe_4$, highlighting the strong anisotropy of the linear compressibility in both studied compounds.

iii. A widely used metric to quantify the degree of elastic anisotropy in crystals is the so-called universal elastic anisotropy A^{U}, defined as follows [61]: $A^{U} = \frac{5G}{G_{\mathrm{R}}} + \frac{B_{\mathrm{V}}}{B_{\mathrm{R}}} - 6$, where B_{V} (G_{V}) and B_{R} (G_{R}) are the estimated values of B (G) according to Voigt and Reuss approximations, respectively. For a perfect isotropic crystal, A^{U} is equal to zero. We never expect perfect isotropic behavior in a crystal; thus, the more the value of A^{U} deviates from zero, the greater the elastic anisotropy of the crystal. The computed value of A^{U} is equal to 0.51 for $Tl_2CdGeSe_4$ and 0.60 for $Tl_2CdSnSe_4$, confirming that the title compounds are characterized by considerable elastic anisotropy.

iv. The percent anisotropy in compression (A_{comp}) and in shear (A_{shear}), defined as $A_{\mathrm{comp}} = ((B_{\mathrm{V}} - B_{\mathrm{R}})/(B_{\mathrm{V}} + B_{\mathrm{R}})) \times 100$ and $A_{\mathrm{shear}} = ((G_{\mathrm{V}} - G_{\mathrm{R}})/(G_{\mathrm{V}}+G_{\mathrm{R}}))\times 100$, where the subscripts V and R denote the Voigt and Reuss limits, respectively, are helpful indicators for estimating the elastic anisotropy in compressibility and in shear, respectively [62]. The degree of deviation of A_{comp} and A_{shear} from 0% mirrors the extent of the elastic anisotropy. In our case, A_{comp} and A_{shear} are equal to 4.0% and 4.6%, respectively, for $Tl_2CdGeSe_4$ and 2.3% and 2.4%, respectively, for $Tl_2CdSnSe_4$. Once again, these indicators highlight the strong elastic anisotropy in the compression and shear of the title compounds.

v. The three-dimensional (3D) representation of the crystal direction dependence of the elastic moduli is the most straightforward method and is widely used to illustrate the degree of elastic anisotropy in crystals. Note that the 3D representation of the crystal direction dependence of the modulus of elasticity is a closed surface, where the distance between the center of that surface and any point on the surface in a given direction is equal to the magnitude of the represented elastic modulus in that direction. Therefore, for an isotropic elastic modulus, the aforementioned closed surface has a perfect spherical shape, and thus, the extent of the deviation of the shape of this surface from the perfect spherical shape reflects the degree of anisotropy of that elastic modulus. In the present study, the elastic anisotropy degree of the $Tl_2CdGeSe_4$ and $Tl_2CdSnSe_4$ crystals was assessed using 3D representations of the directional dependence of Young's modulus (E) and linear compressibility (β). The linear compressibility (β) measures the relative linear shrinkage of a crystal subjected to compression along a given crystallographic direction. The crystal direction-dependent Young's modulus E and linear compressibility β for a tetragonal system are given by the following relationships [63]:

$$\begin{cases} \frac{1}{E} = (l_1^4 + l_2^4)S_{11} + l_3^4 S_{33} + 2l_1^2 l_2^2 S_{12} \\ \qquad +2(l_1^2 l_3^2 + 2l_2^2 l_3^2)S_{13} + (l_2^2 l_3^2 + l_1^2 l_3^2)S_{44} + l_1^2 l_2^2 S_{66} \\ \beta = (S_{11} + S_{12} + S_{13}) - (S_{11} + S_{12} - S_{13} - S_{33})l_3^2 \end{cases}.$$

Here, l_1, l_2 and l_3 are the directional cosines of a given crystal direction in spherical coordinates. The 3D representations of the directional dependence of the linear compressibility (β) and Young's modulus (E) as well as their projections in the $(ac)/(bc)$ and (ab) planes for $Tl_2CdGeSe_4$ and $Tl_2CdSnSe_4$ are shown in Figs. 3 and 4, respectively. Note that the overall topology of the closed surfaces of the Young's modulus and linear compressibility in $Tl_2CdGeSe_4$ are similar to those in $Tl_2CdSnSe_4$. Clearly, the closed surfaces representing the directional dependence of E and β deviate sharply from a spherical shape, mirroring the strong elastic anisotropy of these compounds. To facilitate greater insight into the changes in Young's modulus and linear compressibility along different crystal directions in a plane, we plot the cross-sections of the 3D representations of E and β in the $(ac)/(bc)$ and (ab) ((100)/(010) and (001)) planes in Figs. 2 and 3. These figures demonstrate the considerable deviation of the projections (cross-sections) of the directionally dependent Young's modulus and linear compressibility in the $(ac)/(bc)$ plane from the circular form for both considered compounds, highlighting the strong anisotropy of E and β in this plane, while the cross-sections in the (ab) plane exhibit a perfect circular form for E, highlighting the isotropic character of E in the (ab) plane. The cross-sections of β in the (ab) plane exhibit weak anisotropy. The degree of elastic anisotropy can also be quantified from the relative difference between the minimum and maximum values of the elastic modulus. Figures 2 and 3 show that the linear compressibility of the title compounds reaches the maximum (β_{max}) when the stress is applied along any crystal direction in the (ab) ((001)) plane (note that the linear compressibility is isotropic in the (ab) plane) and is minimum (β_{min}) when the stress is applied along the c-axis, i.e., perpendicular to the (ab) plane. This indicates that when hydrostatic pressure is applied, the contraction of the title crystals that occurs along any direction in the (ab) plane is greater than that occurring along the other crystal directions. The β_{max} of $Tl_2CdGeSe_4$ ($Tl_2CdSnSe_4$) is equal to 18.514 (15.935) TPa^{-1}, and β_{min} is equal to 7.211 (8.028) TPa^{-1}. The difference between β_{max} and β_{min} is noticeable; the former is almost twice the latter, indicating that the linear compressibility is remarkably anisotropic. The Young's modulus value reaches the maximum (E_{max}) when the unidirectional stress is applied along the [001] crystal direction, while it reaches the minimum (E_{min}) when the unidirectional stress is applied along the [111] crystal direction. The E_{max} of $Tl_2CdGeSe_4$ ($Tl_2CdSnSe_4$) is equal to 59.3 (59.9) GPa and the E_{min} is equal to 25.2 (32.6) GPa. These results show that the [001] crystal

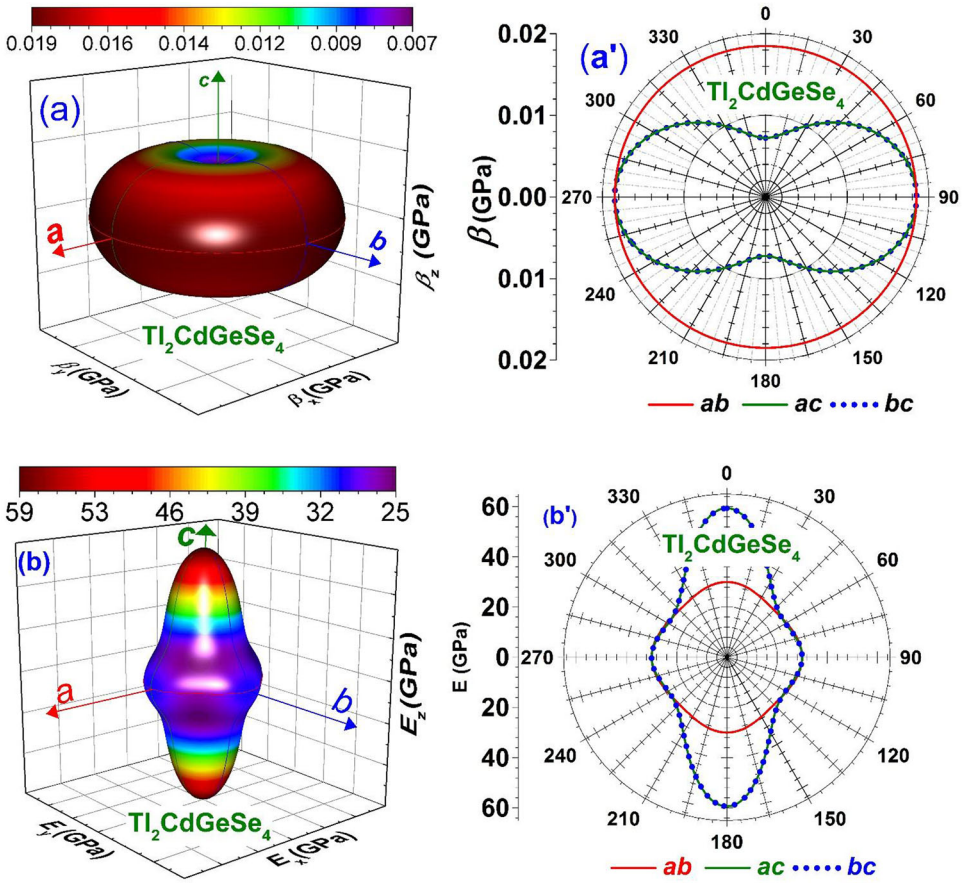

Fig. 3 Directional dependence of the linear compressibility (**a**) and Young's modulus (**b**) and their corresponding cross-sections (**a′**) and (**b′**), respectively; in the (*ab*), (*ac*) and (*bc*) planes for the $Tl_2CdGeSe_4$ compound

direction is more resistant to uniaxial compression than the other crystal directions. This is consistent with the result that C_{33} is the largest elastic constant. The relatively large difference between the E_{max} and E_{min} values, where the former is almost twice the latter, demonstrates the strong anisotropy of Young's modulus. Note that this large difference between the maximum and minimum values of linear compressibility as well as the large difference between the maximum and minimum values of Young's modulus can make the comparison between the theoretical values and the corresponding experimental values slightly complex because the values of these moduli of elasticity depend on the direction of the applied stress with respect to the crystal direction.

3.3 Electrotonic properties

3.3.1 Energy band dispersion

Some key physical parameters, especially those required for optoelectronic devices, such as bandgaps, effective masses of charge carriers, optical coefficients and transport parameters, are calculated from the energy band structure. Therefore, it is crucial to use an accurate theoretical method to correctly describe the energy band dispersions to obtain accurate estimations of the relevant properties. In the present work, the energy band dispersions along the lines joining the high symmetry points in the first Brillouin zone (X–M–Γ–Z–N–P–X) were calculated for $Tl_2CdGeSe_4$ and $Tl_2CdSnSe_4$ in their equilibrium crystal structures using the FP-(L)APW + lo approach within the DFT framework. Both the GGA-PBEsol and TB-mBJ functionals were used to model the exchange–correlation interactions, and calculations were performed both with and without spin–orbit coupling, referenced as + SOC and NSOC, respectively. From the band structure diagrams shown in Fig. 5, we highlight the following characteristics: First, the energy band structure diagrams of the studied compounds are very similar. This is attributed to the fact that these quaternary compounds have identical crystal structures, and three similar component atoms and the different component atoms belong to the same column of the periodic table. Second, the energy levels in the upper valence band at the M and Z points are so close to each other that it is difficult to determine which is the topmost of the valence band without carefully looking at the curve of the upper valence band and examining the numerical values of the energy levels. The numerical values show that the energy level in the upper valence band at the M-point is slightly higher than that at the Z-point for both considered materials, indicating that the valence band maximum (VBM) is located at the M-point for both compounds. As the conduction band minimum (CBM) is also located at the M-point for both compounds,

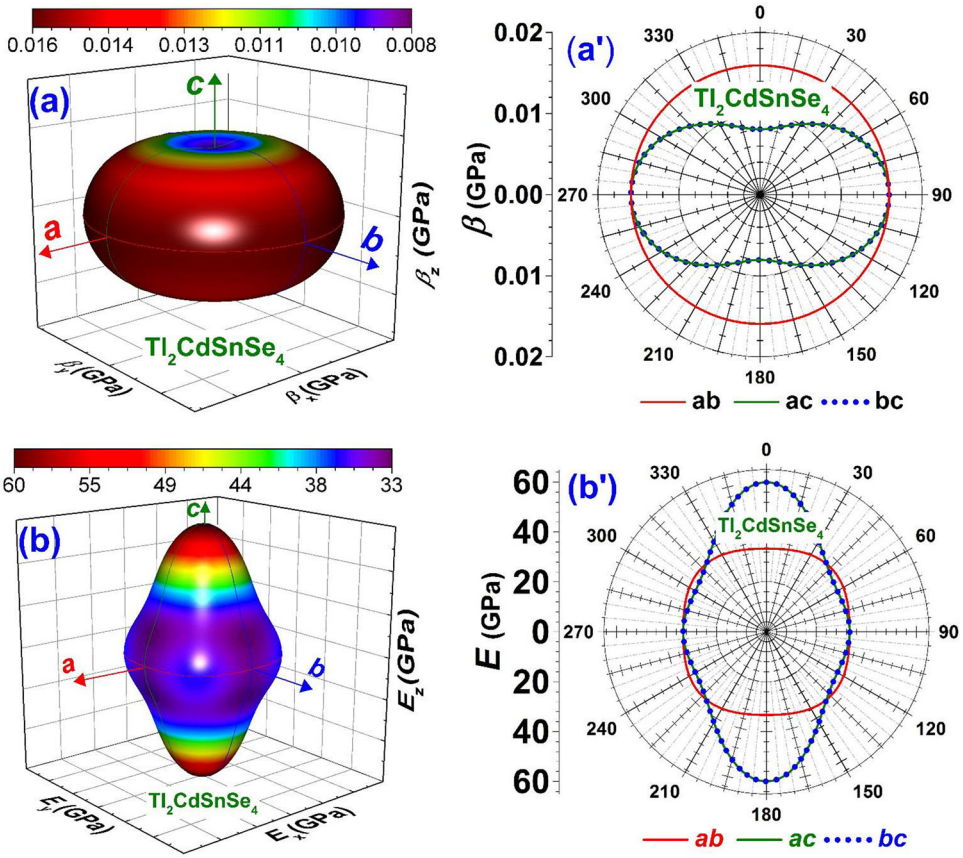

Fig. 4 Directional dependence of the linear compressibility (**a**) and Young's modulus (**b**) and their corresponding cross-sections (**a**′) and (**b**′), respectively; in the (*ab*), (*ac*) and (*bc*) planes for the $Tl_2CdSnSe_4$ compound

Table 7 Calculated electron (m_e^*) and hole (m_h^*) effective masses at the conduction band minimum (CBM, at M-point) and valence band maximum (VBM, at M-point), respectively, towards the Γ and X points in the Brillouin zone

Functional	$Tl_2CdGeSe_4$				$Tl_2CdSnSe_4$			
	m_e^*		m_h^*		m_e^*		m_h^*	
	M → Γ	M → X	M → Γ	M → X	M → Γ	M → X	M → Γ	M → X
GGA08	0.376	0.395	0.344	0.351	0.326	0.343	0.307	0.315
GGA08 + SOC	0.422	0.452	0.346	0.356	0.419	0.457	0.313	0.317
TB-mBJ + SOC	0.732	0.738	0.394	0.402	0.514	0.551	0.351	0.354
TB-mBJ-NSOC	0.542	0.561	0.387	0.392	0.466	0.487	0.348	0.354

we can state that both studied compounds are direct bandgap (M–M) semiconductors. Note that previous calculation results [25, 27] have shown that $Tl_2CdSnSe_4$ is a direct bandgap (M–M) semiconductor [25], which agrees with our findings, while $Tl_2CdGeSe_4$ has been shown to be an indirect bandgap (Z–M) semiconductor [27], which is inconsistent with what we found. To verify our results, the band structure calculation for $Tl_2CdGeSe_4$ was repeated using the PP-PW method as implemented in the CASTEP code [32], and the resulting bandgap character agrees with the results we obtained using the FP-LAPW method. Note that the band structure calculated by Vu et al [27]. also shows that the energy levels in the upper valence band at the M and Z points are so close to each other that it is difficult to tell which is the topmost of the valence band without examining the numerical values of the energy levels. If we take into account that our optimized structural parameters with which the band structure of $Tl_2CdGeSe_4$ was calculated are slightly smaller than those with which Van et al. [27] calculated the band structure (see Table 1), it can therefore be stated that the bandgap may change from the direct type (M–M) to the indirect type (Z–M) depending on the values of the structural parameters with which the band structure is calculated. It should be noted that our optimized structural parameters for $Tl_2CdGeSe_4$ are more in agreement with the corresponding experimental counterparts than those optimized by Van et al. [27] (see Table 6). Third, the energy band around the CBM is slightly less dispersive than that around the VBM, indicating that the electron effective mass is somewhat greater than

Table 6 Calculated energy bandgaps as determined through the GGA-PBEsol and TB-mBJ with (+ SOC) and without (NSOC) including spin–orbit coupling in the present work for the $Tl_2CdGeSe_4$ and $Tl_2CdSnSe_4$ compounds along with available corresponding theoretical and experimental data in the literature

Functional	Bandgap (eV)	
	$Tl_2CdGeSe_4$	$Tl_2CdSnSe_4$
Present		
GG08-NSOC	0.431	0.398
GG08 + SOC	0.305	0. 271
TB-mBJ + SOC	0.981	0.953
TB-mBJ-NSOC	1.123	1.097
Expt. [24]	1.71[1]	1.39[1]
[25]		1.32[1]; 1.29[2]
Calc. [25]		1.143[3]; 1.243[4]

[1]From the absorption coefficient measurements
[2]From the photoconductivity Measurements;
[3]Using the TB-mBJ + SOC
[4]TB-mBJ-NSOC

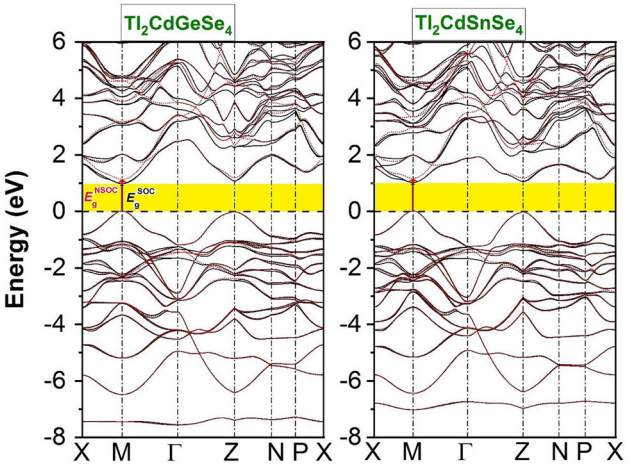

Fig. 5 The calculated TB-mBJ energy band structures for $Tl_2CdGeSe_4$ and $Tl_2CdGeSe_4$ along the $X \rightarrow M \rightarrow \Gamma \rightarrow Z \rightarrow N \rightarrow P \rightarrow X$ k-point path. The VBM and CBM lie both at the M-point, thus both compounds are direct bandgap semiconductors. The black and the dashed-red lines represent the bands calculated with and without spin–orbit coupling, respectively. The zero of energy is chosen to coincide with the top of the valence band. E_g^{SOC} (E_g^{NSOC}) is the fundamental bandgap calculated with SOC (without SOC)

that of the holes. Fourth, the energy band dispersions calculated using GGA08 and TB-mBJ have similar general characteristics, but they are significantly different with regard to the bandgap values. The predicted fundamental bandgaps using GGA08 and TB-mBJ both with and without taking into account spin–orbit coupling are gathered in Table 5 along with available data from the literature [24, 25]. Table 5 shows that the GGA-PBEsol functional seriously underestimates the bandgaps compared to the counterparts provided by the TB-mBJ potential and the experiments [24, 25]. The use of the TB-mBJ potential with the inclusion of SOC widens the bandgap by more than 222% for $Tl_2CdGeSe_4$ and by more than 252% for $Tl_2CdSnSe_4$ compared to the GGA-PBEsol bandgap. Generally, the TB-mBJ potential rigidly pushes the conduction band toward higher energy away from the valence band maximum [64]. Fifth, the inclusion of SOC does not significantly affect the overall appearance of the energy band dispersions; in particular the bands around CBM and VBM are almost unaffected by the inclusion of SOC, as expected from their Se-4p character. The only notable change in the band structure with SOC (+ SOC) is an approximately 13% reduction in the bandgap with respect to that of the counterpart calculated without SOC (NSOC); the CBM shifts to lower energies, thus decreasing the bandgap. Sixth, despite the considerable improvement of the bandgaps when using the TB-mBJ potential compared to the counterparts calculated using GGA-PBEsol, our numerical estimations of the bandgaps remain somewhat smaller than the experimental counterparts [24, 25], by about 35% for $Tl_2CdGeSe_4$ and 20% for $Tl_2CdGeSe_4$. A possible reason for the discrepancy between the theoretical predictions and the corresponding experimental values may be the uncertainties in the measurements. Indeed, even a small uncertainty in the measured spectra of the absorption coefficients from which the reported bandgaps were deduced could cause this discrepancy. Note that the reported bandgaps were evaluated from the tangent of the absorption coefficient at the lower energy and any deviation of the plotting tangent could cause a noticeable deviation in the determined bandgap value. Thus, it is not easy to evaluate the error in the deduced bandgap from the measured absorption coefficient, which justifies why there is no information on the accuracy of the reported experimental data. Furthermore, small differences in the structural parameters could sometimes produce, for the same semiconductor, an appreciable difference in the calculated bandgap, possibly larger than 20% [45]. Note that there is no exchange-energy functional from which the TB-mBJ potential is derived; thus, the calculation of the optimized structural parameters is not possible within the TB-mBJ potential. Additionally, note that sometimes the optical bandgap is larger than the Kohn–Sham bandgap because sometimes the lower energy electronic transitions from the conduction band to valence band could be forbidden according to the selection rules. Further theoretical and experimental studies of the electronic structures of the considered systems are necessary to increase the reliability of both calculations and measurements (Table 6).

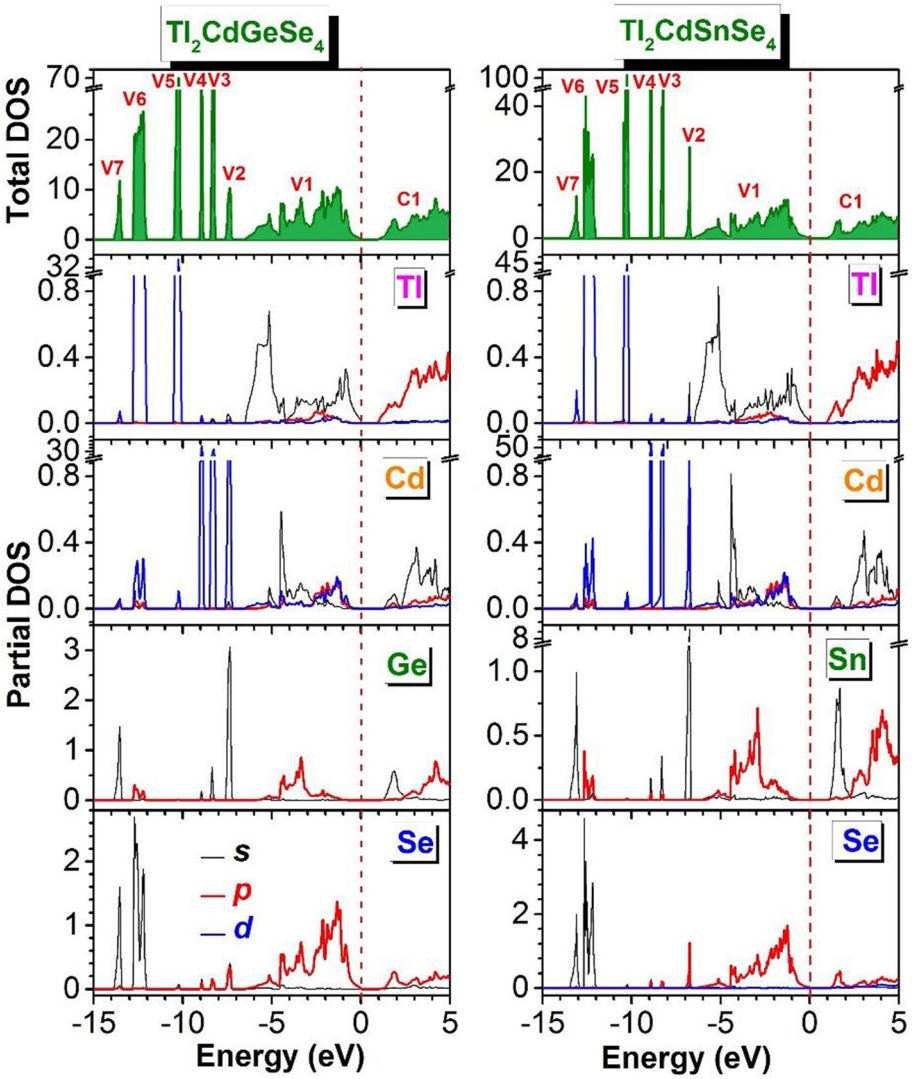

Fig. 6 Total (TDOS, states/eV/primitive-cell) and partial (PDOS; states/eV/atom/orbital) densities of states calculated for $Tl_2CdGeSe_4$ and $Tl_2CdSnSe_4$ crystals using the TB-mBJ potential with spin–orbit coupling

3.3.2 Charge carrier effective masses

The effective masses of charge carriers are key to the transport phenomena in materials. Thus, it is of great importance to estimate the effective masses of charge carriers in semiconductors. The effective mass is a tensor, but it can be treated as a scalar at the extremum of the energy bands. The dispersion of the energy band in the vicinity of its extremum can be adjusted by a parabola: $E(k) = \hbar^2 k^2/2m^*$, where $\hbar$ is Planck's constant and m^* is the charge carrier effective mass. Thus, the charge-carrier m^* can be determined through the following expression: $m^* = \hbar^2(\partial^2 E(k)/\partial^2 k)^{-1}$. The predicted electron and hole effective masses, denoted m_e^* and m_h^*, respectively, at the CBM (located at the M-point) and VBM (located at the M-point), respectively, toward the Γ and X points ($M \rightarrow \Gamma$ and $M \rightarrow X$ directions) in the Brillouin zone are gathered in Table 7. The obtained results reveal that $m_e^* > m_h^*$, which means that the mobility of holes is higher than that of electrons. The effective masses of electrons and holes exhibit a very weak anisotropy; the electron and hole effective masses toward the $M \rightarrow \Gamma$ direction are approximately equal to the corresponding masses toward the $M \rightarrow X$ direction. The inclusion of SOC in the calculations somewhat increases the electron and hole effective masses (Fig. 5).

3.3.3 Density of states

To determine the origin of the electronic states forming the valence and conduction energy levels of the quaternary selenides $Tl_2CdGeSe_4$ and $Tl_2CdGeSe_4$, the total density of states (TDOS) and l-projected atomic-resolved density of states (PDOS) were calculated using the TB-mBJ potential with SOC. As seen in Fig. 6, the valence bands are regrouped in seven subbands denoted V1, V2, V3, V4, V5, V6 and V7. The V7, V6, V5, V4, V3 and V2 subbands are somewhat isolated, lying in narrow energy windows far from the upper valence band group V1. To shorten the text, the results relating to $Tl_2CdSnSe_4$ are given in brackets hereafter. The V7

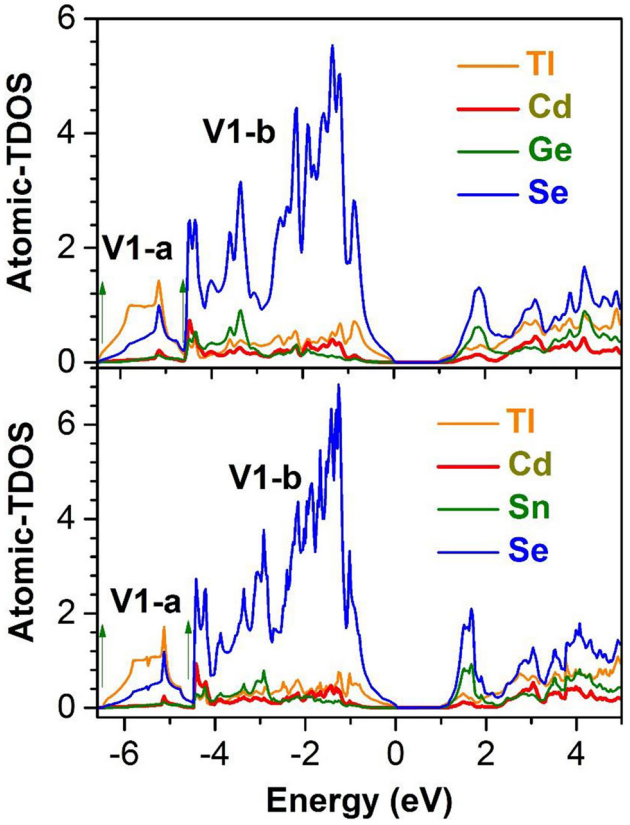

Fig. 7 The atomic total densities of states (TDOS) in the upper valence subband for the $Tl_2CdGeSe_4$ and $Tl_2CdSnSe_4$ compounds

subband, centered at − 13.5 (− 13.1) eV, comes from the Ge-4s (Sn-5s) and Se-4s states. The V6 subband, covering the energy range of − 12.9 to − 12.02 (− 12.7 to − 12.03) eV, is dominated by the contribution of the Tl-5d states, with a small contribution from the Se-4s states. The Tl-5d states form the V5 subband, peaking at − 10.2 (− 10.3) eV. The V4 subband, peaking at − 8.9 (− 8.9) eV, is composed of the Cd-4d states. The V3 band group, centered at − 8.3 (− 8.2) eV, is derived from the Cd-4d states. The V2 subband, centered at − 7.4 (− 6.8) eV, is a mixture of the Cd-4d and Ge-4s (Sn-5s) orbitals. As seen in Fig. 7, the upper valence band group V1, ranging from approximately − 6.5 (− 6.5) up to the Fermi level, is subdivided into two parts: V1-a and V1-b. The lower part, V1-a, ranging from approximately − 6.5 (− 6.5) eV to − 4.6 (− 4.5) eV, is composed of the hybridized Tl-6s and Se-4p states. The upper part, V1-b, ranging from approximately − 4.6 (− 5.5) eV to the Fermi level, is mainly associated with the Se-4p states, with a very small contribution from the Tl-6s, Cd-5s and Ge-4p (Sn-5p) states. This is quite consistent with the Se^{2-}, Tl^{1+} (the p shell is empty), Cd^{2+} and Ge^{4+}/Sb^{4+} oxidation states, suggesting that the Se–Tl, Se–Cd and Se–Ge (Sn) bonds predominantly exhibit ionic characteristics. In addition, the Se–Cd, Se–Tl and Se–Ge (Se–Sn) bonds are expected to have some degree of covalency due to weak hybridization between the Se-4p and Cd-5s states, between the Se-4p and Tl-6s states and between the Se-4p and Ge-4p (Sn-5p) orbitals, respectively. The edge of the conduction band (the bottom of the C1 conduction subband) is mainly from the empty Se-4p and Ge-4s (Sn-5s) states, while the remainder of C1 is made up of a mixture of the Sn-sp, Cd-s, Tl-p and Se-p states, indicating that not all Se ions are saturated. Interestingly, in the case of $Tl_2CdGeSe_4$, the Se-4p states, which are the main contributors to the valence band, are positioned mainly in the upper part of the valence band and substantially in its central portion, while the main contributions of the Ge-4p states are in the central portion of the valence band. These theoretical findings are in excellent agreement with the experimental measurements of the energy distribution of the Se-4p and Ge-4p states in $Tl_2CdGeSe_4$ [27].

3.4 Frequency-dependent optical functions

Figure 8 shows the spectra of the components of the imaginary part of the optical complex dielectric function, viz., $\varepsilon_2^{xx}(\omega)$ and $\varepsilon_2^{zz}(\omega)$, where $\varepsilon_2^{xx}(\omega)$ and $\varepsilon_2^{zz}(\omega)$ characterize the absorption of the energy of incident electromagnetic waves with an electric field vector $\vec{E}$ polarized parallel to the a-axis ($\vec{E}//\vec{a}$) and the c-axis ($\vec{E}//\vec{c}$), respectively. As clearly seen in the aforementioned figure, the $\varepsilon_2(\omega)$ spectra of both compounds exhibit notable anisotropy: (i) the general characteristics of the spectra of the $\varepsilon_2^{xx}(\omega)$ and $\varepsilon_2^{zz}(\omega)$ components are remarkably distinct from each other throughout the considered energy window; (ii) the number and positions of the major peaks and structures in the $\varepsilon_2^{xx}(\omega)$ spectrum are noticeably different from those in the $\varepsilon_2^{zz}(\omega)$ spectrum; and (iii) the amplitudes of the main peaks and structures of the $\varepsilon_2^{zz}(\omega)$ spectrum are remarkably higher than those of the $\varepsilon_2^{xx}(\omega)$ spectrum. It is of fundamental interest to attempt to determine the microscopic origin of the electronic transitions between the occupied valence band states and the empty conduction band states that give rise to the peaks and structures of the $\varepsilon_2^{xx}(\omega)$ and $\varepsilon_2^{zz}(\omega)$ spectra based on the band structure and density of state diagrams. For this purpose, the ε_2^{xx} and ε_2^{zz} spectra were decomposed into the individual contributions of the electronic transitions between pairs of bands, $V_n \rightarrow C_{n'}$, where V_n is a valence band of index n and $C_{n'}$ is a conduction band of index n'. Once the pair of bands $(V_n, C_{n'})$ has been determined, we determine the wave vectors k of the electronic states that mainly contribute to the interband transition $V_n \rightarrow C_{n'}$ from the $(C_{n'} - V_n)(k)$ dispersion. Tables 8, 9, 10 and 11 list the energetic positions of the main peaks (Pi) of the $\varepsilon_2^{xx}(\omega)$ and $\varepsilon_2^{zz}(\omega)$ spectra, the pairs of bands $(V_n, C_{n'})$ that dominantly contribute to the peaks and structures of the spectra and the electronic states involved in each interband direct transition $V_n \rightarrow C_{n'}$. Furthermore, based on the TDOS and PDOS diagrams, the main contributions to the $\varepsilon_2^{xx}(\omega)$ and $\varepsilon_2^{zz}(\omega)$ spectra in the energy range of 0–6 eV are the allowed direct interband electronic transitions from

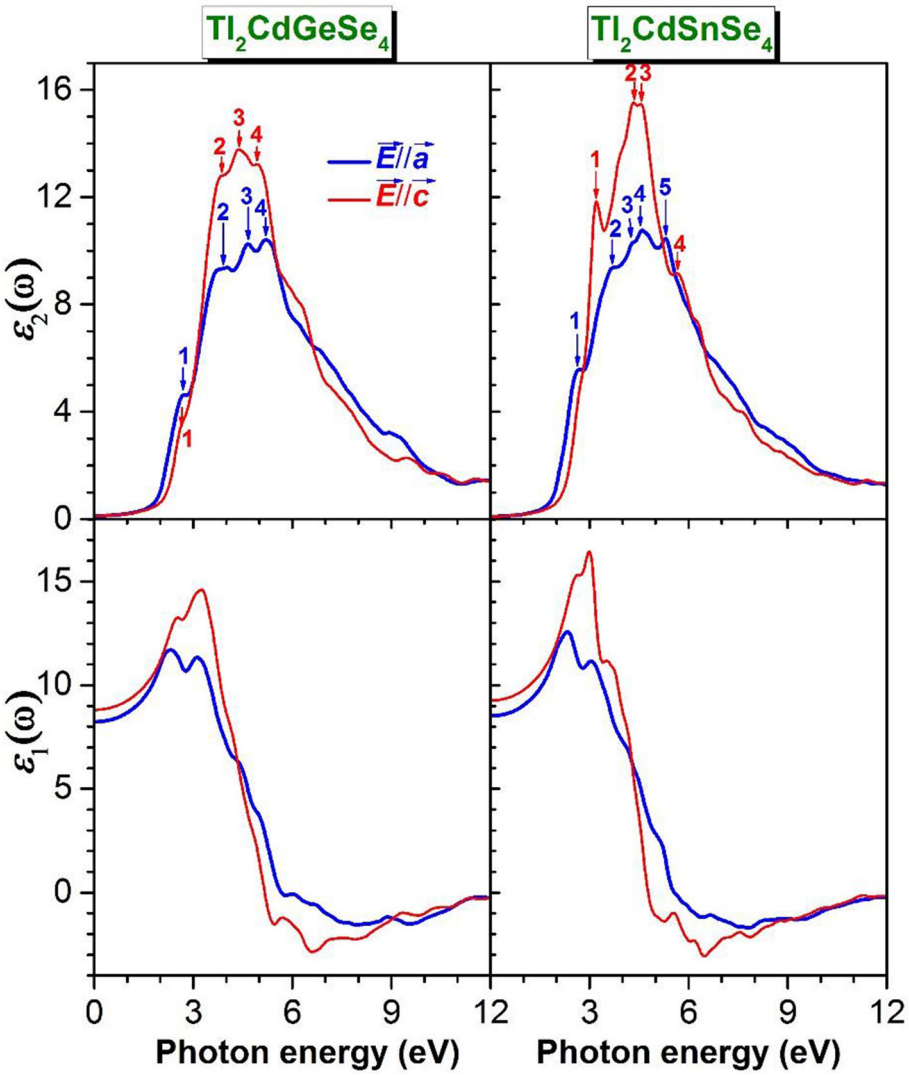

Fig. 8 Frequency-dependent curves of the real ($\varepsilon_1(\omega)$) and imaginary ($\varepsilon_2(\omega)$) parts of the dielectric function for incident electromagnetic radiation polarized parallel to the a- and c-axes for the $Tl_2CdGeSe_4$ and $Tl_2CdSnSe_4$ materials. The critical point structures (peaks) are pointed out by the label i ($i = 1, 2, 3\ldots$)

the valence subband V1 to the conduction subband C1. This evidence shows that the optical structures in the energy range of 0–6 eV in the $\varepsilon_2^{xx}(\omega)$ and $\varepsilon_2^{zz}(\omega)$ curves of the studied compounds mainly originate from the direct electronic transitions from the Se-4p occupied valence states to the Se-4p, Ge-4s (Sn-5s), Cd-5s and Tl-6p empty conduction states.

Figure 8 shows that the general characteristics of the $\varepsilon_1^{xx}(\omega)$ and spectra $\varepsilon_1^{zz}(\varepsilon)$(components of the real part of the dielectric function) are remarkably different, indicating the strong anisotropy of this optical property of the considered compounds. The peak amplitudes of the $\varepsilon_1^{zz}(\varepsilon)$ spectrum are significantly higher than those of the $\varepsilon_1^{xx}(\omega)$ spectrum. The static components of the electronic part of the static dielectric constant $\varepsilon(0)$, an optical parameter of crucial importance for optoelectronic devices, can be deduced from the limits of the $\varepsilon_1^{xx}(\omega)$ and $\varepsilon_1^{zz}(\omega)$ spectra when $\omega \to 0$. The estimated values of $\varepsilon^{xx}(0) = \varepsilon_1^{xx}(0) = \varepsilon_1^{xx}(\omega \to 0)$ and $\varepsilon^{zz}(0) = \varepsilon_1^{zz}(0) = \varepsilon_1^{zz}(\omega \to 0)$ are approximately equal to 8.23 and 8.82, respectively, for $Tl_2CdGeSe_4$ and 8.51 and 9.26, respectively, for $Tl_2CdSnSe_4$. The $\varepsilon^{xx}(0)$ and $\varepsilon^{zz}(0)$ values of $Tl_2CdSnSe_4$ are slightly greater than those of $Tl_2CdGeSe_4$. This trend is consistent with Penn's model [65], which claims that a larger bandgap corresponds to a smaller static dielectric constant. The available data in the literature for the components of the static real part of the dielectric function for the $Tl_2CdSnSe_4$ compound ($\varepsilon_1^{xx}(0) = 14$ and $\varepsilon_1^{zz}(0) = 16.0$) [25] are almost double the values we obtained ($\varepsilon_1^{xx}(0) = 8.51$ and $\varepsilon_1^{zz}(0) = 9.26$). By comparing the magnitudes of our calculated $\varepsilon_2^{xx}(\omega)$ and $\varepsilon_2^{zz}(\omega)$ spectra with those reported in the literature [25], we notice that the magnitudes of the reported $\varepsilon_2^{xx}(\omega)$ and $\varepsilon_2^{zz}(\omega)$ spectra for $Tl_2CdSnSe_4$ are almost double those of our spectra. To check the reliability of our results, we recalculated the $\varepsilon_2^{xx}(\omega)$ and $\varepsilon_2^{zz}(\omega)$ spectra of $Tl_2CdSnSe_4$ using another computer code based on another ab initio method, and the obtained results are consistent with our previous results. A probable reason for the discrepancy between our results and those reported in the literature is that the results reported

Table 8 Peak positions of the ε_2^{xx} spectrum together with the dominant interband transition contributions to every peak and their location in the Brillouin zone for $Tl_2CdGeSe_4$. The counting of the bands is down (up) from the top (bottom) of the valence (conduction) band

Optical structure		Dominant interband transition contributions			
Peak	Position	Transition	BZ Region	Percentage	Position
P1	2.66	V_1–C_1	M–Γ–X; P–N	13.9	2.64
		V_1–C_2	X–M–Γ; X–P	2.2	2.64
		V_2–C_1	X–M–Γ; X–P	14.0	2.55
		V_3–C_1	X–M–Γ	2.1	2.66
P2	3.91	V_1–C_2	M–Γ–X–P–N–Γ	2.45	3.26
		V_1–C_3	M–Γ–X–P	8.28	3.66
		V_2–C_2	M–Γ–X; P–N–Γ	3.49	3.69
		V_3–C_1	M–Γ–X; P–N	2.36	3.11
		V_3–C_2	M–Γ–X–P–N–Γ	2.17	4.08
		V_4–C_1	X–M–Γ; X–P	3.10	3.02
		V_4–C_2	M–Γ–X–P–N–Γ	3.60	3.99
		V_5–C_1	X–M–Γ	6.39	3.21
		V_5–C_2	X–M–Γ–X–P–N–Γ	2.40	4.18
		V_6–C_1	M–Γ–X–P	4.86	3.99
		V_6–C_2	X–M–Γ–X–P–N–Γ	1.51	4.08
		V_7–C_1	X–M–Γ; X–P	2.47	4.08
P3	4.63	V_1–C_5	M–Γ–X–P; N–Γ	2.54	4.92
		V_1–C_6	X–M–Γ; X–P	5.34	4.82
		V_2–C_3	M–Γ–X–P	7.68	4.27
		V_2–C_4	M–Γ–Γ–X–P–N	5.51	4.86
		V_3–C_3	M–Γ–X–P; N–Γ	4.19	4.66
		V_1–C_4	M–Γ–X–P–N–Γ	3.41	4.57
		V_3–C_4	X–M–Γ–X–P–N–Γ	4.02	4.96
P4	5.20	V_1–C_6	M–Γ–X–P–N–Γ	4.33	5.11
		V_2–C_5	M–Γ–X–P; N–Γ	4.23	5.15
		V_2–C_6	X–M–Γ	3.95	5.35
		V_2–C_7	X–M–Γ–X–P	3.95	5.73
		V_3–C_5	X–M–Γ	3.39	5.15
		V_3–C_6	X–M–Γ–X–P–N–Γ	4.05	5.54
		V_4–C_4	M–Γ–X–P–N–Γ	2.14	5.24
		V_4–C_6	M–Γ–X–P–N–Γ	2.92	5.82
		V_5–C_4	M–Γ–X–P–N–Γ	2.18	5.54
		V_6–C_4	X–M–Γ–X–P	2.76	5.44
		V_9–C_1	M–Γ–X; P–N	3.31	5.15

[25] were obtained using a relatively old version of the WIEN2k code, where the doubling of the number of energy bands upon inclusion of SOC is not taken into account when calculating optical properties. If the doubling of the number of energy bands when including SOC is not taken into account, the magnitude of the imaginary part of the dielectric function ($\varepsilon_2(\omega)$) is doubled, which has repercussions on the optical parameters deduced from $\varepsilon_2(\omega)$, such as the real part of the dielectric function ($\varepsilon_2(\omega)$) and all other optical functions.

The absorption coefficient $\alpha(\omega)$, which is an important optical parameter quantifying the fraction of energy of incident radiation of frequency ω absorbed per unit length when it passes through a medium, is a key parameter in terms of possible implications of a semiconductor in optoelectronic devices. The calculated $\alpha^{xx}(\omega)$ and $\alpha^{zz}(\omega)$ spectra, components of the absorption coefficient $\alpha(\omega)$ that correspond to incident electromagnetic radiation polarized parallel to the *a*- and *c*-axes, respectively, are illustrated in Fig. 9a. Both

Table 9 Peak positions of the ε_2^{zz} spectrum together with the dominant interband transition contributions to every peak and their location in the Brillouin zone for $Tl_2CdGeSe_4$. The counting of the bands is down (up) from the top (bottom) of the valence (conduction) band

Optical structure		Dominant interband transition contributions			
Peak	Position	Transition	BZ region	Percentage	Position
E1	2.65	V_1–C_1	M–Γ–X; P–N	4.71	2.74
		V_2–C_1	X–M–Γ; X–P	16.07	2.56
		V_3–C_1	X–M–Γ	3.76	2.51
E2	3.84	V_1–C_2	M–Γ–X–P–N–Γ	1.86	3.80
		V_2–C_2	M–Γ–X–P–N–Γ	4.46	3.90
		V_3–C_1	M–Γ–X; P–N	3.13	3.19
		V_3–C_2	M–Γ–X–P–N–Γ	4.0	3.90
		V_4–C_1	M–Γ–X; P–N	5.35	3.47
		V_4–C_2	M–Γ–X–P–N–Γ	2.25	3.96
		V_5–C_1	X–M–Γ; X–P	6.54	3.41
		V_6–C_1	M–Γ–X–P	3.81	3.85
E3	4.38	V_1–C_5	X–M–Γ; X–P	4.35	4.62
		V_2–C_3	M–Γ–X–P	5.72	4.27
		V_3–C_3	M–Γ–X–P	8.56	4.50
		V_5–C_2	M–Γ–X–P–N–Γ	2.19	4.69
		V_5–C_3	X–M–Γ–X–P	2.88	4.72
		V_6–C_2	M–Γ–X–P–N–Γ	4.61	4.59
		V_7–C_1	X–M–Γ; X–P	3.31	4.18
		V_8–C_1	X–M–Γ; X–P–N	4.33	4.72
E4	4.93	V_1–C_6	M–Γ–X–P–N–Γ	2.41	5.10
		V_2–C_4	M–Γ–X–P–N–Γ	2.61	4.86
		V_3–C_4	M–Γ–X–P–N–Γ	2.61	4.97
		V_3–C_5	X–M–Γ–X–P	3.05	5.17
		V_4–C_4	M–Γ–X–P	3.17	4.87
		V_4–C_5	M–Γ–X–P–N–Γ	2.46	5.49
		V_5–C_5	X–M–Γ–X–P–N–Γ	2.26	4.95
		V_6–C_3	X–M–Γ–X–P	2.83	5.21
		V_7–C_2	M–Γ–X–P; N	5.51	4.93
		V_9–C_1	M–Γ–X; P–N	2.84	5.16

the $\alpha^{xx}(\omega)$ and $\alpha^{zz}(\omega)$ curves consist of one structure extending from the absorption edge, which corresponds to the lower allowed electronic interband direct transition, up to the considered energy range. The $\alpha^{xx}(\omega)$ and $\alpha^{zz}(\omega)$ spectra start to increase sharply from the same absorption edge but at different rates; the $\alpha^{xx}(\omega)$ spectrum grows more rapidly than the $\alpha^{zz}(\omega)$ curve. Figure 9b clearly shows that in the low energy range (lower than 3.25 eV for $Tl_2CdGeSe_4$ and lower than 2.92 eV for $Tl_2CdGeSe_4$), the amplitude of the $\alpha^{xx}(\omega)$ spectrum is slightly higher than that of the $\alpha^{zz}(\omega)$ spectrum, indicating that the edge of the bandgap is somewhat anisotropic. The amplitudes of the $\alpha(\omega)$ spectra of the studied compounds are higher than 10^4 cm^{-1} in an energy range including the visible spectrum and higher than 10^5 cm^{-1} in a wide energy window extending approximately from 2.34 (2.53) eV up to the considered energy range (20 eV) in the case of $Tl_2CdGeSe_4$ for $\vec{E}//\vec{a}(\vec{E}//\vec{c})$ and from 2.28 (2.52) eV up to the considered energy range in the case of $Tl_2CdSnSe_4$ for $\vec{E}//\vec{a}(\vec{E}//\vec{c})$, suggesting that these materials could be potential candidates for optoelectronic devices operating in a wide energy range from the visible spectrum to the UV range. The $\alpha(\omega)$ spectrum reaches a maximum magnitude of approximately 1.5×10^6 cm^{-1} at approximately 6.5 eV in both studied materials for $\vec{E}//\vec{c}$.

Table 10 Peak positions of the ε_2^{xx} spectrum together with the dominant interband transition contributions to every peak and their location in the Brillouin zone for $Tl_2CdSnSe_4$. The counting of the bands is down (up) from the top (bottom) of the valence (conduction) band

Optical structure		Dominant interband transition contributions			
Peak	Position	Transition	Region	Percentage	Position
P1	2.7	V_1–C_1	M–Γ–X; P–N	14.49	2.57
		V_2–C_1	X–M–Γ–X–P–N	15.75	2.73
P2	3.7	V_1–C_2	M–Γ–X–P; N–Γ	2.61	3.79
		V_1–C_3	M–Γ–X–P	4.15	3.34
		V_2–C_2	X–M–Γ–X–P	4.15	3.1
		V_3–C_1	M–Γ–X; N–Γ	6.03	3.14
		V_4–C_1	M–Γ–X; P–N	5.57	3.20
		V_5–C_1	X–M–Γ; X–P	4.74	3.10
		V_6–C_1	X–M–Γ–X–P	9.56	3.61
		V_7–C_1	X–M–Γ	2.95	3.79
P3	4.29	V_1–C_3	M–Γ–X–P; N–Γ	3.59	4.13
		V_2–C_3	M–Γ–X–P	7.94	4.28
		V_3–C_2	M–Γ–X–P–N–Γ	2.64	4.19
		V_4–C_2	M–Γ–X–P–N–Γ	3.45	3.95
		V_8–C_1	X–M–Γ; X–P–N	3.44	4.32
P4	4.65	V_1–C_4	M–Γ–X–P–N–Γ	4.81	4.55
		V_1–C_5	M–Γ–X–P; N–Γ	2.31	4.88
		V_1–C_6	M–Γ–X–P	2.57	4.73
		V_2–C_4	M–Γ–X–P–N–Γ	4.98	4.80
		V_3–C_3	M–Γ–X–P; N–Γ	4.15	4.58
		V_3–C_4	M–Γ–X–P, N–Γ	3.35	4.89
		V_4–C_3	M–Γ–X–P; N–Γ	2	4.79
		V_9–C_1	X–M–Γ; X–P–N	2.35	4.60
P5	5.34	V_1–C_6	M–Γ–X–P; N–Γ	2.86	5.14
		V_1–C_7	X–M–Γ; X–P, N–Γ	2.19	5.49
		V_1–C_8	X–M–Γ	2.09	5.24
		V_2–C_5	M–Γ–X–P; N–Γ	2.76	5.05
		V_2–C_6	X–M–Γ–X–P–N–Γ	6.53	5,31
		V_2–C_7	X–M–Γ; X–P; N–Γ	3.3	5.66
		V_3–C_5	M–Γ–X–P	3.13	5.13
		V_3–C_6	X–M–Γ	4.74	5.36
		V_4–C_4	M–Γ–X–P–N–Γ	2.29	5.06
		V_4–C_5	M–Γ–X–P	2.19	5.33
		V_4–C_6	M–Γ–X–P–N–Γ	3.17	5.70
		V_5–C_4	M–Γ–X–P–N–Γ	3.2	5.44
		V_5–C_6	X–M–Γ–X–P	3.19	5.74
		V_6–C_4	X–M–Γ–X–P	3.75	5.29
		V_6–C_6	X–M–Γ–X–P	3.9	5.99

Table 11 Peak positions of the ε_2^{zz} spectrum together with the dominant interband transition contributions to every peak and their location in the Brillouin zone for $Tl_2CdSnSe_4$. The counting of the bands is down (up) from the top (bottom) of the valence (conduction) band

Optical structure		Dominant interband transition contributions			
Peak	Position	Transition	Region	Percentage	Position
P1	3.2	V_2–C_1	M–Γ–X; N–Γ	9.70	3.02
		V_2–C_2	X–M–Γ–X–P	3.46	3.12
		V_3–C_1	M–Γ–X; N–Γ	22.02	3.13
		V_4–C_1	M–Γ–X; P–N	16.45	3.21
		V_5–C_1	X–M–Γ; X–P	8.78	3.19
P2	3.92	V_3–C_2	M–Γ–X–P–N–Γ	4.02	4.02
		V_4–C_2	M–Γ–X–P–N–Γ	2.84	3.93
		V_5–C_2	X–M–Γ–X–P	1.90	3.96
		V_6–C_1	X–M–Γ–X–P	5.79	3.62
		V_6–C_2	X–M–Γ–X–P	5.88	4.06
		V_7–C_1	X–M–Γ; X–P	4.80	3.80
P3	4.32	V_1–C_3	M–Γ–X–P	1.99	4.12
		V_1–C_5	X–M–Γ; X–P	1.78	4.30
		V_2–C_3	M–Γ–X–P	6.5	4.27
		V_2–C_4	X–M–Γ–X–P	2.34	4.45
		V_3–C_3	M–Γ–X–P	5.03	4.33
		V_5–C_2	M–Γ–X–P–N–Γ	2.16	4.33
P4	4.55	V_1–C_4	M–Γ–X–P–N–Γ	2	4.55
		V_4–C_4	X–M–Γ–X–P	3.49	4.77
		V_5–C_3	X–M–Γ–X–P	2	4.9
		V_6–C_3	M–Γ–X–P, N–Γ	3.72	5.24
		V_7–C_2	M–Γ–X–P–N–Γ	3.77	4.70
		V_8–C_1	M–Γ–X; N–Γ	6.84	4.84
		V_9–C_1	X–M–Γ; X–P–N	4.66	4.63
P5	5.64	V_2–C_7	X–M–Γ; X–P, N–Γ	3.42	5.67
		V_3–C_6	M–Γ–X–P–N–Γ	2.17	5.55
		V_4–C_6	M–Γ–X–P	2.28	5.60
		V_5–C_6	X–M–Γ; X–P–N–Γ	3.37	5.72
		V_6–C_4	M–Γ–X–P	2.27	5.69
		V_{11}–C_1	M–Γ–X; P–N	4.13	5.83

Figure 9b represents the frequency-dependent curves of $n^{xx}(\omega)$ and $n^{zz}(\omega)$, components of the refractive index $n(\omega)$, another important optical parameter describing the refraction of electromagnetic radiation propagating through a medium [66]. Figure 9b obviously shows that the refractive indices $n(\omega)$ of both investigated compounds are considerably anisotropic. The static components, $n^{xx}(0)$ and $n^{zz}(0)$, of the static refractive index, $n(0)$, are equal to 2.88 (2.93) and 2.98 (3.05), respectively, for $Tl_2CdGeSe_4$ ($Tl_2CdSnSe_4$). The $n^{xx}(\omega)$ spectrum exhibits two summa, $n^{xx}_{summ-1}(\omega) = 3.46$ (3.60) at 2.38 (2.38) eV and $n^{xx}_{summ-2}(\omega) = 3.50$ (3.49) at 3.24 (3.16) eV for $Tl_2CdGeSe_4$ ($Tl_2CdSnSe_4$), while $n^{zz}(\omega)$ exhibits one summum, $n^{zz}_{summ}(\omega) = 3.98(4.20)$ at 3.31 (3.05) eV four $Tl_2CdGeSe_4$ ($Tl_2CdSnSe_4$).

The frequency-dependent curves of the components of the optical reflectivity $R(\omega)$, namely, $R^{xx}(\omega)$ and $R^{zz}(\omega)$, of the title compounds are shown in Fig. 9c. It is noted that the $R(\omega)$ spectra of $Tl_2CdGeSe_4$ and $Tl_2CdSnSe_4$ are characterized by a notable anisotropy in the energy range of 0–9 eV; the amplitude of $R^{zz}(\omega)$ is clearly higher than that of $R^{xx}(\omega)$ in this energy window. The amplitudes of the $R^{xx}(\omega)$ and $R^{zz}(\omega)$ spectra become too close and decrease rapidly toward zero value in the energy range of 10–20 eV. The components of the static reflectivity, viz., $R^{xx}(0)$ and $R^{zz}(0)$, are equal to approximately 23 (24)% and 25 (26)%, respectively, for $Tl_2CdGeSe_4$ ($Tl_2CdSnSe_4$). The optical reflectivity $R^{zz}(\omega)$ is higher than 40% in a large energy window expanding from approximately 3.5 eV to approximately 8.9 eV.

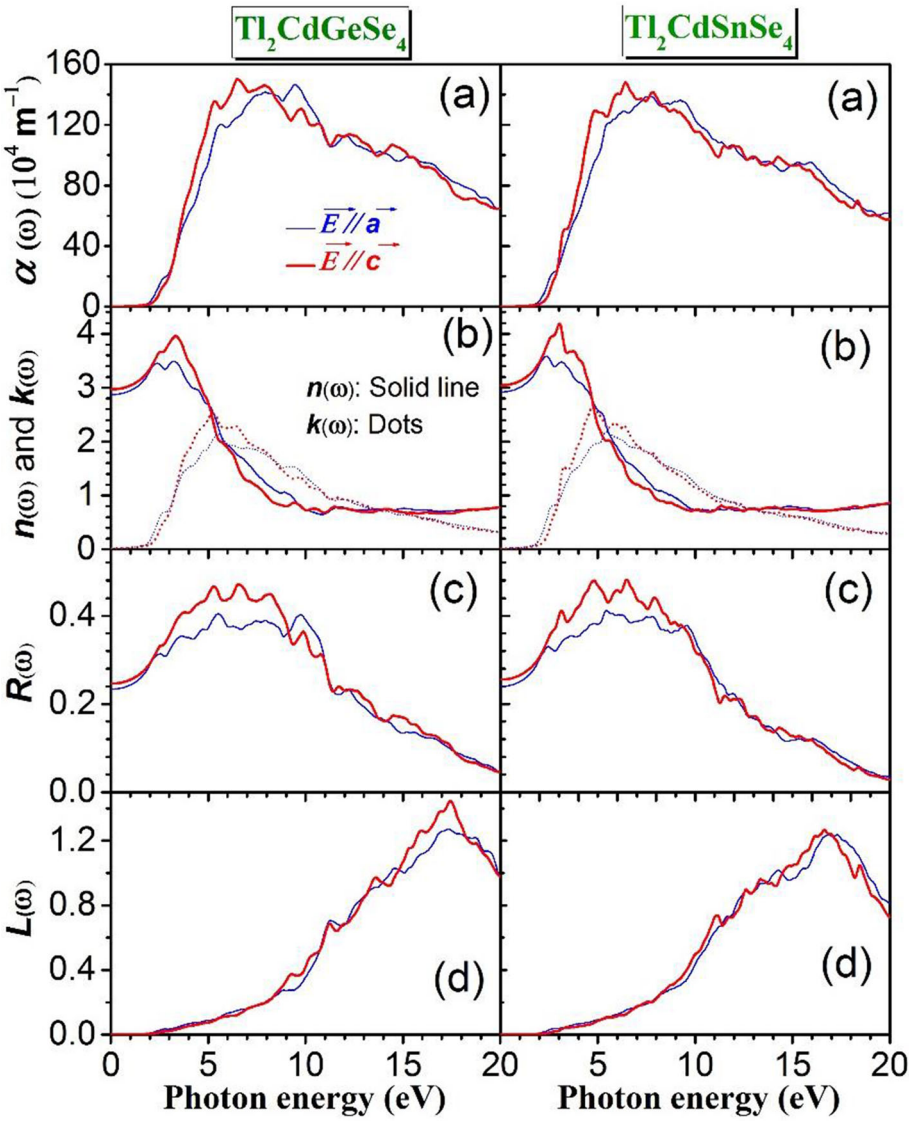

Fig. 9 Calculated frequency-dependent curves of **a** the absorption coefficient $\alpha(\omega)$, **b** refractive index $n(\omega)$ and extinction coefficient $k(\omega)$, **c** reflectivity $R(\omega)$ and **d** energy-loss function $L(\omega)$ for the $Tl_2CdGeSe_4$ and $Tl_2CdSnSe_4$ materials

The spectra of $L^{xx}(\omega)$ and $L^{zz}(\omega)$, components of the electron energy-loss function $L(\omega)$, an optical parameter describing the energy lost by fast electrons traversing a homogeneous dielectric material, are illustrated in Fig. 9d. The main peak of $L(\omega)$ spectra is usually associated with the plasma frequency ω_p. The $L^{xx}(\omega)$ and $L^{zz}(\omega)$ spectra exhibit a maximum centered at approximately 17.5 (16.7) eV, which is associated with the plasma oscillations in $Tl_2CdGeSe_4$ ($Tl_2CdSnSe_4$). The main structures in the $L^{xx}(\omega)$ and $L^{zz}(\omega)$ spectra correspond to the trailing edges in the $R^{xx}(\omega)$ and $R^{zz}(\omega)$ spectra, respectively.

4 Conclusion

The main conclusions that we can draw from our detailed systematic ab initio investigation of the structural, elastic, electronic and optical properties of the considered quaternary thallium selenide systems are as follows:

(i) The optimized structural parameters are in excellent agreement with the experimental counterparts, confirming the reliability of the theoretical method used to predict the physical properties of the title compounds.
(ii) Analysis of the monocrystalline elastic constants reveals that the investigated materials are mechanically stable, soft and substantially structurally and elastically anisotropic.
(iii) Analysis of the energy band dispersions and the density of states diagrams shows that the studied materials are direct bandgap semiconductors, the upper valence band dominantly originates from the Se-4*p* states, and the Se-Tl, Se-Cd, Se-Ge and Se-Sn bonds dominantly have ionic character with a certain degree of covalency. The TB-mBJ potential considerably improves the

bandgap value, but it is still somewhat smaller than its experimental counterpart. Inclusion of the spin–orbit coupling reduces the bandgap.

(iv) The frequency-dependent linear optical functions, viz., complex dielectric function, refractive index, optical reflectivity and energy-loss function, were determined for incident photons with energies between 0 and 20 eV. The studied materials exhibit a high absorption in an energy window involving the visible spectrum. A tentative analysis was performed to determine the microscopic origin of the observed optical structures in the imaginary part of the dielectric function.

Acknowledgements The author S. Bin-Omran acknowledges the Researchers Supporting Project number RSP-2021/82, King Saud University, Riyadh, Saudi Arabia.

Author contributions

SK: conceptualization, methodology, writing—original draft, AB: investigation, writing—review and editing, DA: methodology, KH: data curation, SB-O: resources, RK: software, YA-D: supervision, AFH: visualization, AH: validation, AFAE-R: validation.

References

1. A. Gutzmann, C. Nather, W. Bensch, K4Vp2S9. Acta Cryst. C **60**, i11–i13 (2004)
2. S. Kumar, A. Akande, F. El-Mellouhi, H. Park, S. Sanvito, Theoretical investigation of the structural, elastic, electronic, and dielectric properties of alkali-metal-based bismuth ternary chalcogenides. Phys. Rev. Mater. **4**, 075401–075413 (2020)
3. R. Kanno, T. Hata, Y. Kawamoto, M. Irie, Synthesis of a new lithium ionic conductor, thio-LISICON–lithium germanium sulfide system. Solid State Ion. **130**, 97–104 (2000)
4. B.N. Schumer, R.T. Downs, K.J. Domanik, M.B. Andrade, M.J. Origlieri, Pirquitasite, Ag_2ZnSnS_4. Acta Cryst. E **69**, i8–i9 (2013)
5. Yu. Kogut, A. Fedorchuk, O. Zhbankov, Ya. Romanyuk, I. Kityk, L. Piskach, O. Parasyuk, Isothermal section of the Ag_2S–PbS–GeS_2 system at 300 K and the crystal structure of Ag_2PbGeS_4. J. Alloys Compd. **509**, 4264–4267 (2011)
6. Y. Huang, K. Wu, J. Cheng, Y. Chu, Z. Yang, S. Pan, Li_2ZnGeS_4: a promising diamond-like infrared nonlinear optical material with high laser damage threshold and outstanding second-harmonic generation response. Dalton Trans. **48**, 4484–4488 (2019)
7. D.-Y. Chung, T. Hogan, P. Brazis, M. Rocci-Lane, C. Kannewurf, M. Bastea, C. Uher, M.G. Kanatzidis, $CsBi_4Te_6$: a high-performance thermoelectric material for low-temperature applications. Science **287**, 1024–1027 (2000)
8. M.G. Brik, O.V. Parasyuk, G.L. Myronchuk, I.V. Kityk, Specific features of band structure and optical anisotropy of $Cu_2CdGeSe_4$ quaternary compounds. Mater. Chem. Phys. **147**, 155–161 (2014)
9. A.P. Litvinchuk, V.M. Dzhagan, V.O. Yukhymchuk, M. YaValakh, I.S. Babichuk, O.V. Parasyuk, L.V. Piskach, O.D. Gordan, D.R.T. Zahn, Electronic structure, optical properties and lattice dynamics of orthorhombic Cu_2CdGeS_4 and Cu_2CdSiS_4 semiconductors. Phys. Rev. B **90**(16), 165201–165208 (2014)
10. C. Rincon, M. Quintero, E. Moreno, E. Ch Power, J.A. Quintero, M.A. Henao, Macías, Raman spectrum of $Cu_2CdSnSe_4$ stannite structure semiconductor compound. Superlattices Microstruct. **88**, 99–103 (2015)
11. J.-H. Zhang, D.J. Clark, A. Weiland, S.S. Stoyko, Y.S. Kim, J.I. Jang, J. Aitken, $Li_2CdGeSe_4$ and $Li_2CdSnSe_4$: biaxial nonlinear optical materials with strong infrared second-order responses and laser-induced damage thresholds influenced by photoluminescence. Inorg. Chem. Front. **4**, 1472–1484 (2017)
12. L. Salik, A. Bouhemadou, K. Boudiaf, F. Saad Saoud, S. Bin-Omran, R. Khenata, Y. Al-Douri, A.H. Reshak, Structural, elastic, electronic, magnetic, optical, and thermoelectric properties of the diamond-like quaternary semiconductor $CuMn_2InSe_4$. J. Supercond. Nov. Magn. **33**, 1091–1102 (2020)
13. S. Alnujaim, A. Bouhemadou, A. Bedjaoui, S. Bin-Omran, Y. Al-Douri, R. Khenata, S. Maabed, Ab initio prediction of the elastic, electronic and optical properties of a new family of diamond-like semiconductors, Li_2HgMS_4 (M = Si, Ge and Sn). J. Alloys Compd. **843**, 155991–156014 (2020)
14. A. Bedjaoui, A. Bouhemadou, S. Aloumi, R. Khenata, S. Bin-Omran, Y. Al-Douri, F. Saad Saoud, S. Bensalem, Structural, elastic, electronic and optical properties of the novel quaternary diamond-like semiconductors Cu_2MgSiS_4 and Cu_2MgGeS_4. Solid State Sci. **70**, 21–35 (2017)
15. N. Greenwood, A. Earnshaw, *Chemistry of the Elements* (Pergamon Press, Elmsford, 1984)
16. M.A. McGuire, T.K. Reynolds, F.J. DiSalvo, Exploring thallium compounds as thermoelectric materials: seventeen new thallium chalcogenides. Chem. Mater. **17**, 2875–2884 (2005)
17. M.A. McGuire, T.J. Scheidemantel, J.V. Badding, F.J. DiSalvo, Tl_2AXTe_4 (A = Cd, Hg, Mn; X = Ge, Sn): crystal structure, electronic structure, and thermoelectric properties. Chem. Mater. **17**, 6186–6191 (2005)
18. A.A. Lavrentyev, B.V. Gabrelian, T.V. Vu, L.N. Ananchenko, G.L. Myronchuk, O.V. Parasyuk, V.A. Tkach, K.I. Kopylova, O.Y. Khyzhun, Electronic and optical properties of quaternary sulfide Tl_2HgSnS_4, a promising optoelectronic semiconductor: a combined experimental and theoretical study. Opt. Mater. **92**, 294–302 (2019)
19. A.O. Selezen, L.V. Piskach, O.V. Parasyuk, I.D. Olekseyuk, The Tl_2SnSe_3-CdSe system and the crystal structure of the $Tl_2CdSnSe_4$ compound. J. Phase Equilib. Diffus. **40**(6), 797–801 (2019)

20. MYu. Mozolyuk, L.V. Piskach, A.O. Fedorchuk, I.D. Olekseyuk, O.V. Parasyuk, Physico-chemical interaction in the Tl_2Se–HgSe–$DIVSe_2$ systems (DIV – Si, Sn). Mater. Res. Bull. **47**, 3830–3834 (2012)
21. M. Yu Mozolyuk, L.V. Piskach, A.O. Fedorchuk, I.D. Olekseyuk, O.V. Parasyuk, The Tl2Se–HgSe–$GeSe_2$ system and the crystal structure of $Tl_2HgGeSe_4$. Chem. Met. Alloys. **6**, 55–62 (2013)
22. L.V. Piskach, M. Yu Mozolyuk, A.O. Fedorchuk, I.D. Olekseyuk, O.V. Parasyuk, Phase equilibria in the Tl_2S–HgS–SnS_2 system at 520 K and crystal structure of Tl_2HgSnS_4. Chem. Met. Alloys **10**, 136–141 (2017)
23. V. Vu, A.A. Lavrentyev, B.V. Gabrelian, H.D. Tong, O.V. Parasyuk, O.Y. Khyzhun, Calculations within DFT framework of the electronic and optical properties of quaternary sulfide Tl_2PbSiS_4, a prospective optoelectronic semiconductor. Comput. Condens. Matter **21**, e00392-11 (2019)
24. A.O. Selezen, I.D. Olekseyuk, G.L. Myronchuk, O.V. Smitiukh, L.V. Piskach, Synthesis and structure of the new semiconductor compounds $Tl_2B^{II}D^{IV}X_4$ (B^{II}–Cd, Hg; D^{IV}–Si, Ge; X–Se, Te) and isothermal sections of the Tl_2Se–CdSe–Ge(Sn)Se_2 systems at 570 K. J. Solid State Chem. **289**, 121422–121427 (2020)
25. T.V. Vu, A.A. Lavrentyev, B.V. Gabrelian, A.O. Selezen, L.V. Piskach, G.L. Myronchuk, M. Denysyuk, V.A. Tkach, K.D. Pham, O.Y. Khyzhun, Crystal growth, electronic and optical properties of $Tl_2CdSnSe_4$, a recently discovered prospective semiconductor for application in thin film solar cells and optoelectronics. Opt. Mater. **111**, 110656–110712 (2021)
26. O.V. Parasyuk, V.S. Babizhetskyy, O.Y. Khyzhun, V.O. Levytskyy, I.V. Kityk, G.L. Myronchuk, O.V. Tsisar, L.V. Piskach, J. Jedryka, A. Maciag, M. Piasecki, Novel quaternary $TlGaSn_2Se_6$ single crystal as promising material for laser operated infrared nonlinear optical modulators. Curr. Comput.-Aided Drug Des. **7**, 341–416 (2017)
27. T.V. Vu, A.A. Lavrentyev, B.V. Gabrelian, A.O. Selezen, L.V. Piskach, I.D. Olekseyuk, G.L. Myronchuk, M. Denysyuk, V.A. Tkach, N.N. Hieu, K.D. Pham, O.Y. Khyzhun, Quaternary $Tl_2CdGeSe_4$ selenide: electronic structure and optical properties of a novel semiconductor for potential application in optoelectronics. J. Solid State Chem. **302**, 122453–122513 (2021)
28. O.Y. Khyzhun, V.L. Bekenev, V.V. Atuchin, L.D. Pokrovsky, V.N. Shlegel, N.V. Ivannikova, The electronic structure of Pb_2MoO_5: first-principles DFT calculations and X-ray spectroscopy measurements. Mater. Des. **105**, 315–322 (2016)
29. P.K. Bayannavar, A.C. Mendhe, B.R. Sankapal, M.S. Sannaikar, S.K.J. Shaikh, S.R. Inamdar, R.R. Kamble, Synthesis of metal free organic dyes: experimental and theoretical approach to sensitize one-dimensional cadmium sulphide nanowires for solar cell application. J. Mol. Liq. **336**, 116862–116869 (2021)
30. B. Pandit, S.R. Rondiya, S. Shegokar, L.K. Bommineedi, R.W. Cross, N.Y. Dzade, B.R. Sankapal, Reciprocated electrochemical and DFT investigations of iron selenide: mechanically bendable solid-state symmetric supercapacitor. Sustain. Energy Fuels **5**, 5001–5012 (2021)
31. S. Majumder, P.K. Baviskar, B.R. Sankapal, Straightening of chemically deposited CdS nanowires through annealing towards improved PV device performance. Ceram. Int. **42**, 6682–6691 (2016)
32. S.J. Clark, M.D. Segall, C.J. Pickard, P.J. Hasnip, M.J. Probert, K. Refson, M.C. Payne, First principles methods using CASTEP. Z. Kristallogr. **220**, 567–570 (2005)
33. J.P. Perdew, A. Ruzsinszky, G.I. Csonka, O.A. Vydrov, G.E. Scuseria, L.A. Constantin, X. Zhou, K. Burke, Restoring the density-gradient expansion for exchange in solids and surfaces. Phys. Rev. Lett. **100**, 136406–136414 (2008)
34. J.S. Lin, A. Qteish, M.C. Payne, V. Heine, Optimized and transferable nonlocal separable ab initio pseudopotentials Phys. Rev. B **47**, 4174–4180 (1993)
35. S.B. Zhang, L.W. Shi, Comput. Mater. Sci. **142**, 99 (2018)
36. H.J. Monkhorst, J.D. Pack, Special points for Brillouin-zone integrations. Phys. Rev. B **13**, 5188–5192 (1976)
37. B.G. Pfrommer, M. Côté, S.G. Louie, M.L. Cohen, Relaxation of crystals with the quasi-Newton method. J. Comput. Phys. **131**, 233–240 (1997)
38. S. Baroni, S. de Gironcoli, A. Dal Corso, P. Giannozzi, Phonons and related crystal properties from density-functional perturbation theory. Rev. Mod. Phys. **73**, 515–562 (2001)
39. P. Blaha, K. Schwarz, F. Tran, R.T. Laskowski, G.K.H. Madsen, L.D. Marks, WIEN2k: an APW+lo program for calculating the properties of solids. J. Chem. Phys. **152**, 074101–074130 (2020)
40. F. Tran, P. Blaha, Accurate band gaps of semiconductors and insulators with a semilocal exchange-correlation potential. Phys. Rev. Lett. **102**, 226401–226404 (2009)
41. D. Koller, F. Tran, P. Blaha, Improving the modified Becke–Johnson exchange potential. Phys. Rev. B **85**, 155109 (2012)
42. K.S. Virdi, Y. Kauffmann, C. Ziegler, P. Ganter, B.V.L. Wayne, D. Kaplan, P. Blaha, C. Scheu, Electronic structure of $KCa_2Nb_3O_{10}$ as envisaged by density functional theory and valence electron energy loss spectroscopy. Phys. Rev. B **87**, 115108–115109 (2013)
43. C.-Y. Yoo, K.-P. Hong, S.-J. Kim, A new-layered perovskite, $KSrNb_2O_6F$, by powder neutron diffraction. Acta Crystallogr. Sect. C Cryst. Struct. Commun. **63**, i63–i65 (2007)
44. D. Koller, F. Tran, P. Blaha, Merits and limits of the modified Becke-Johnson exchange potential. Phys. Rev. B **83**, 195134–195210 (2011)
45. D.J. Singh, S.S.A. Seo, H.N. Lee, Optical properties of ferroelectric $Bi_4Ti_3O_{12}$. Phys. Rev. B **82**, 180103(R) – 180104 (2010)
46. J.A. Camargo-Martinez, R. Baquero, Performance of the modified Becke–Johnson potential for semiconductors. Phys. Rev. B **86**, 195106–195108 (2012)
47. C. Ambrosch-Draxl, J.O. Sofo, Linear optical properties of solids within the full-potential linearized augmented planewave method. Comput. Phys. Commun. **175**, 1–14 (2006)
48. F. Mouhat, F.-X. Coudert, Necessary and sufficient elastic stability conditions in various crystal systems. Phys. Rev. B **90**, 224104–224114 (2014)

49. R. Hill, The elastic behavior of a crystalline aggregate. Proc. Phys. Soc. A **65**, 349–354 (1952)
50. A. Bedjaoui, A. Bouhemadou, S. Bin-Omran, Structural, elastic and thermodynamic properties of tetragonal and orthorhombic polymorphs of Sr_2GeN_2: an ab initio investigation. High Press. Res. **36**, 198–219 (2016)
51. Z. Wu, E. Zhao, H. Xiang, X. Hao, X. Liu, J. Meng, Crystal structures and elastic properties of superhard IrN_2 and IrN_3 from first principles. Phys. Rev. B **76**, 054115–054215 (2007)
52. Y. Tian, B. Xu, Z. Zhao, Microscopic theory of hardness and design of novel superhard crystals. Int. J. Refract. Hard Met. Hard Mater. **33**, 93–106 (2012)
53. Q.-J. Liu, Z.-T. Liu, L.-P. Feng, Elasticity, electronic, chemical bonding and optical properties of monoclinic ZrO_2 from first-principles. Phys. B **406**, 345–350 (2011)
54. S. Chen, Y. Sun, Y.-H. Duan, B. Huang, M.-J. Peng, Phase stability, structural and elastic properties of C15-type Laves transition-metal compounds MCo_2 from first-principles calculations. J. Alloys Compd **630**, 202–208 (2015)
55. S. Pugh, Relations between the elastic moduli and the plastic properties of polycrystalline pure metals. Philos. Mag. **7**, 823–843 (1954)
56. S.K. Saha, G. Dutta, Elastic and thermal properties of the layered thermoelectrics BiOCuSe and LaOCuSe. Phys. Rev. B **94**, 125209–125218 (2016)
57. O.L. Anderson, A simplified method for calculating the Debye temperature from elastic constants. J. Phys. Chem. Solids **24**, 909–917 (1963)
58. E. Langenberg, E. Ferreiro-Vila, V. Leborán, A.O. Fumega, V. Pardo, F. Rivadulla, Analysis of the temperature dependence of the thermal conductivity of insulating single crystal oxides. Appl. Phys. Lett. Mater. **4**, 104815–104819 (2016)
59. P. Ravindran, L. Fast, P.A. Korzhavyi, B. Johansson, Density functional theory for calculation of elastic properties of orthorhombic crystals: application to $TiSi_2$. J. Appl. Phys. **84**, 4891–4904 (1998)
60. H. Ledbetter, A. Migliori, A general elastic-anisotropy measure. J. Appl. Phys. **100**, 063516–063525 (2006)
61. D.-D. Pang, X.-Q. Huang, H.-Y. Xue, C. Zhang, Z.-L. Lv, M.-Y. Duan, Properties of a predicted tetragonal carbon allotrope: first principles study. Diam. Relat. Mater. **82**, 50–55 (2018)
62. S.I. Ranganathan, M. Ostoja-Starzewski, Universal Elastic Anisotropy Index. Phys. Rev. Lett. **101**, 055504–055514 (2008)
63. D.H. Chung, W.R. Buessem, in: *Anisotropy in Single Crystal Refractory Compounds*, vol. 2, ed. by F.W. Vahldiek, S.A. Mersol (Plenum Press, New York, 1968), pp. 217–245
64. J.F. Nye, *Properties of Crystals* (Oxford University Press, Oxford, 1985)
65. O. Boudrifa, A. Bouhemadou, Ş Uğur, R. Khenata, S. Bin-Omran, Y. Al-Douri, Structural, electronic, optical and elastic properties of the complex K_2PtCl_6-structure hydrides $ARuH_6$ (A = Mg, Ca, Sr and Ba): first-principles study. Philos. Mag. **96**, 2328–2361 (2016)
66. D.R. Penn, Wave-number-dependent dielectric function of semiconductors. Phys. Rev. **128**, 2093 (1960)